On the colloidal and molecular aspects of peptide self-assembly

Rüter, Axel

2020

Document Version:
Publisher's PDF, also known as Version of record

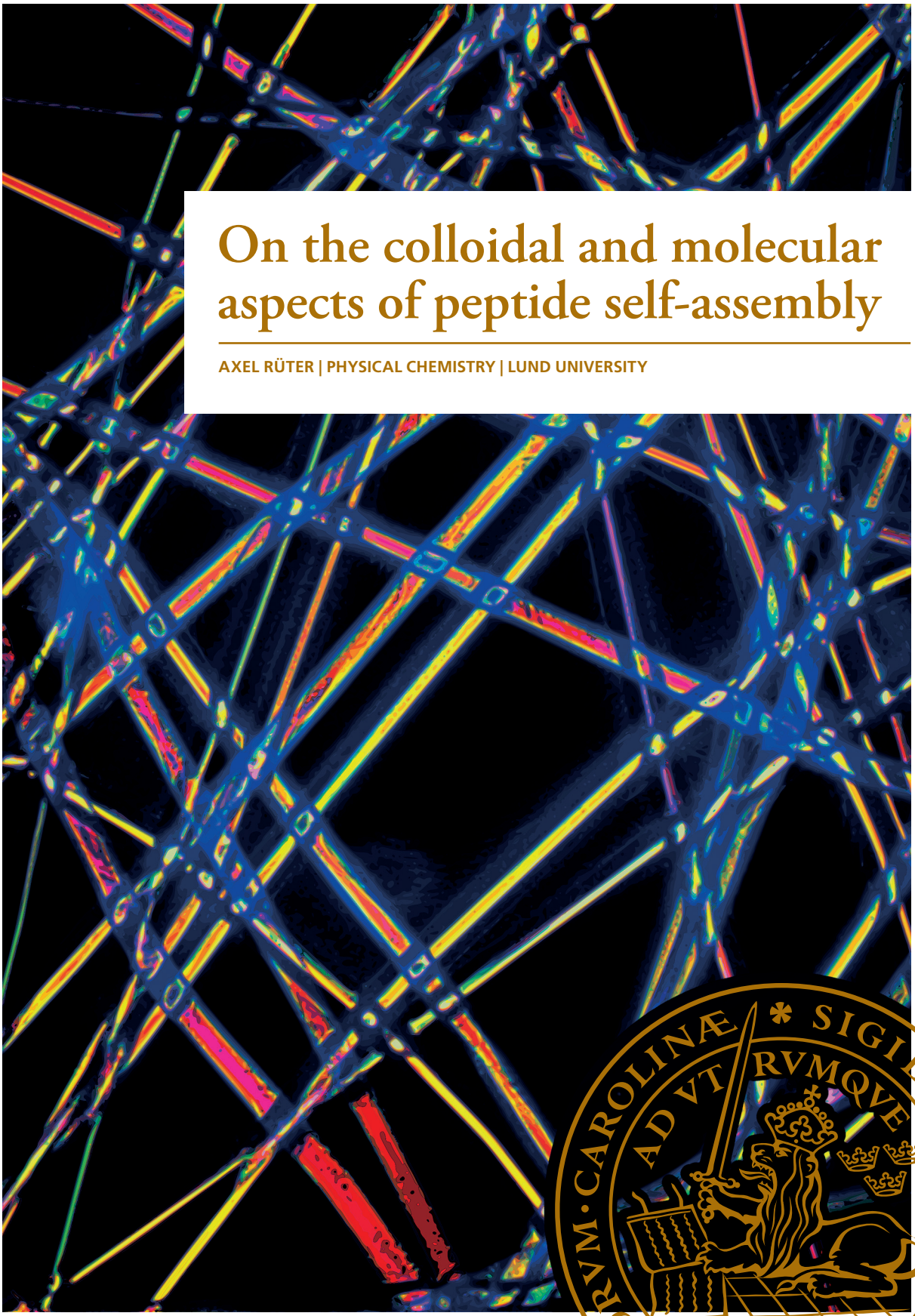

On the colloidal and molecular aspects of peptide self-assembly

AXEL RÜTER | PHYSICAL CHEMISTRY | LUND UNIVERSITY

On the colloidal and molecular aspects of peptide self-assembly

On the colloidal and molecular aspects of peptide self-assembly

by Axel Rüter

LUND
UNIVERSITY

DOCTORAL DISSERTATION

by due permission of the Faculty of Science, Lund University, Sweden.
To be defended on Friday, the 6th of March 2020 at 09:15 in Lecture hall B at the Department of Chemistry, Lund University.

Faculty opponent

Dr. Joel Schneider
National Institutes of Health NIH, U.S.A.

Organization
LUND UNIVERSITY

Department of Chemistry
Box 124
SE–221 00 LUND
Sweden

Author(s)
Axel Rüter

Document name
DOCTORAL DISSERTATION

Date of disputation
2020-03-06

Sponsoring organization
Knut and Alice Wallenberg Foundation
Grant number: KAW 2014.0052

Title and subtitle
On the colloidal and molecular aspects of peptide self-assembly:

Abstract

Peptide self-assembly is a spontaneous process, ubiquitous in nature for the creation of highly ordered and complex biological structures, making it a sought after technique in the development of novel biocompatible materials. The process is also strongly associated with various neurodegenerative diseases in the formation of amyloid plaques in diseases such as Alzheimer's and Parkinson's, where fully functioning proteins aggregate are re-assembled into non-functional fibrillar aggregates that eventually lead to cell death. Understanding the underlying thermodynamics and kinetics of peptide assembly can therefore not only support the material science community, but might also lead to a deeper knowledge of biological phenomena.

In this thesis we have studied the self-assembly of the A_nK model peptide, where n denotes the number of the hydrophobic amino acid alanine, A, and K is lysine that is hydrophilic. Whereas the shorter A_6K assembles into hollow nanotubes, the longer A_8K and $A_{10}K$ instead assemble into amyloid-like twisted ribbons. Although the structures macroscopically differ, using X-ray and electron microscopy techniques, we show that both structures consist of the same crystalline monlayers of laminated β-sheets. From the gained structural knowledge we have devised a simple thermodynamic model describing the structures and the transition between them with increasing n.

We have further characterized the kinetics of the A_8K and $A_{10}K$ self-assembly using NMR, spectroscopic and calorimetric techniques. The kinetics of attachment and detachment is strikingly slow. We propose that this is a general feature of β-sheet aggregates. Solutions of A_8K and $A_{10}K$ ribbons were also investigated by rheology. The ribbons behave like charged rods, forming a highly viscous glassy state at higher concentration. Finally it is determined that similar self-assembly as in water is formed in methanol and dimethylformamide.

Key words
Peptide self-assembly, aggregation kinetics, peptide hydrogel, small angle scattering, rheology

Classification system and/or index terms (if any)

Supplementary bibliographical information

Language
English

ISSN and key title

ISBN
978-91-7422-722-2 (print)
978-91-7422-723-9 (pdf)

Recipient's notes

Number of pages
188

Price

Security classification

Signature 

Date 2020-01-22

On the colloidal and molecular aspects of peptide self-assembly

by Axel Rüter

LUND
UNIVERSITY

This doctoral thesis is constructed as a summary of research papers and consists of two parts. An introductory text puts the research work into context and summarizes the main conclusions of the papers. Then, the research publications themselves are reproduced. The research papers may either have been already published or are manuscripts at various stages.

Cover photo front: An imaging spacer in polarized microscopy.

Cover illustration back: A word cloud created at wordclouds.com.

Faculty of Science, Department of Chemistry, Division of Physical Chemistry

ISBN: 978-91-7422-722-2 (print)
ISBN: 978-91-7422-723-9 (pdf)

Printed in Sweden by Media-Tryck, Lund University, Lund 2020

Media-Tryck is a Nordic Swan Ecolabel certified provider of printed material. Read more about our environmental work at www.mediatryck.lu.se

MADE IN SWEDEN

If you wish to make an apple pie from scratch,
you must first invent the universe.

- Carl Sagan

Table of Contents

Acknowledgments v
Populärvetenskaplig Sammanfattning vii
List of Publications ix
Author Contributions x
Abbreviations xi

Prologue **1**

1 Introduction **3**

1.1 Amino acids, peptides, proteins 4
1.2 Peptide self-assembly and thermodynamics 5
1.3 Self-assembling peptide systems 6

2 Methods **11**

2.1 Static scattering 12
2.2 Dynamic scattering 16
2.3 Rheology 17
2.4 Nuclear magnetic resonance 20
2.5 Isothermal titration calorimetry 21
2.6 Transmission electron microscopy 22
2.7 Circular dichroism 24

3 Structure & Thermodynamics **27**

3.1 Aqueous self-assembly 28
3.2 Structure models 32
3.3 Free energy models 34
3.4 Non-aqueous assembly 37
3.5 Conclusions 39

4 Kinetics of assembly and dissolution **41**

4.1 The assembly process 42
4.2 Aggregate dissolution 45
4.3 Peptide deprotonation upon assembly 48
4.4 Conclusions 49

5 Peptide fibrils as rigid rods **51**

5.1 Dynamical arrest and viscoelastic behavior 52
5.2 Rod interactions 55
5.3 Liquid crystal transition 58
5.4 Flow behavior 60
5.5 Conclusions 60

6 Epilogue **63**

Scientific Publications **75**

Acknowledgments

The book you are holding in your hand might only be printed with a single name on it, but it is far from a one-man job. First and foremost, I would like to thank my main supervisor, **Ulf**. Thank you, for always keeping me on my toes and challenging me to keep on learning. Thank you, for always supporting me, and the rest of the group for that matter, also outside of the scientific scope. There are so many non-scientific components of a PhD project and I am grateful that you care about everything. I would also like to extend a thank you to my secondary supervisor, **Mikael**. Thank you for being available for discussion whenever I needed.

I would like to thank the great collaborators we have had over the various projects. Thank you, **Darrin**, for giving me the opportunity to spend a couple of months in your lab, thank you, **Joakim**, for all the helpful input on thinking and writing theoretical chemistry, thank you, **Narayan** and **Thomas**, for the expert help with synchrotron data acquisition and analysis, thank you, **Kevin**, for expert input on the alignment experiments, and thank you, **Alessandra**, for the amazing work and your tremendous drive behind everything you do.

I would like to give my sincerest appreciation to the permanent staff of the division and the department. Thank you, **Maria S.**, for making sure that we are safe and well equipped, **Helena** and **Maria L.**, for keeping such good track of way too many absent-minded scientists, **Chris W.**, for an endless supply of drill bits, glue and digital storage space, **Paula**, for checking all my figures at 400 % zoom or more, **Anna**, for assisting me to visualize incredibly small things, and finally, **Peter H.**, for assistance in dealing with furious Indian gods.

The scientific workplace is a very dynamic and the amount of people that crosses your path during a PhD is staggering. When I first came to the division, I was given a warm welcome by my first office mates: **Marta**, **Weimin** and **Joel**. Thank you for explaining the ins and outs of the division and for helping me get started with the daily life as a PhD student. I could not have gotten a better start and I have tried to hold the colorful flag high ever since you left. **Luigi** and **Stefan**, with both of you around, there was no way that this was going to go wrong. Thank you for always being available for questions, for sharing all your incredible knowledge and for the good collaborative spirit that has resulted in our common work. Thank you, **Birte**, for sharing all your expertise and tips, and for help in the last minute madness of creating this book. Thank you also to the rest of the group (present and past): **Jon**, **Marija**, **Viktoriia**, **Vero**, **Erika**, **Brett**, **Ana**, **Mona**, **Alfred** and **Marcus** for all the joyful moments in the office and for continuously cheering me on during the various parts of my work.

Working at the Division of Physical Chemistry would not have been the same without the warm including environment, which I hope will continue for as long as the KC building stands. Specifically, the willingness to share and discuss topics from high to low over a nice and warm (not always delicious though) cup of coffee. A heartfelt thank you to my most immediate PhD brothers and sisters: **Tommy G.**, **Maria V.**, **Maxime**, **Jasper**, **Linda**, **João**, **Vicky**, **Johan**, **Polina** and **Dora**. Sharing this journey with you all has been incredible. Thank you, **Thiago**, **Niels**, **Dat**, **Felix**, **Arif** and **Antara** for always being cheerful and creating an incredible workspace.

I am very thankful to have had the support of a group of heartwarming friends throughout all my 10 years in Lund: **Martin**, **Calle**, **Fredrik**, **Helena**, **Elin**, **Elina**. I wish our friendship never ends. Also the rest of the Dr. Nano group with whom I have enjoyed most of my Friday lunches, and where we have been able to discuss and compare the highs and the lows of PhD-ing, you all deserve an honorable mention: **Malin**, **Marcus**, **Mårten**, **Joel**, **Axel**, **Emil**, **Anders** and **Sara**. I will see you on the other side!

Finally, I would like to give a huge, loving thank you to my family, who is always there whenever needed. Thank you for always believing in me and for pushing me to do what I want to do and be who I want to be. And **Isabelle**, there are not enough words to describe how thankful I am to have you in my life. We have already enjoyed a bunch of amazing adventures, but there is also soon more to come!

Populärvetenskaplig Sammanfattning

Molekyler i lösning kan spontant gå samman och bilda välordnade strukturer utan extern påverkan. I naturen är detta ett välanvänt koncept för tillverkning av olika material och strukturer. Många bra exempel på sådana material återfinns i den mänskliga kroppen, exempelvis de membran som omsluter alla våra celler eller vårt DNA som sitter i en dubbel helixstrukturer. Självaggregering förekommer även inom vissa sjukdomsförlopp, till exempel Alzheimers och Parkinsons, där proteiner i hjärnan självaggregerar till långa fiberlika strukturer som helt saknar funktion och leder till celldöd.

Drivkraften bakom den spontana processen självaggregering är att minimera systemets fria energi. Fri energi är ett koncept inom termodynamiken och kan beskrivas som ett mått på hur gärna ett system genomgår förändring. Ju högre energi ett system har desto mer sannolikt är det att genomgå förändring. Därför har ett termodynamiskt stabilt system låg fri energi. I självaggregering av hydrofoba (feta) molekyler minimeras den fria energin i första hand genom den så kallade hydrofoba effekten. Vissa molekyler är amfifila (d.v.s både hydrofoba och hydrofila). De kan aggregera så att de hydrofoba delarna göms bakom de hydrofila. Förutom den hydrofoba effekten finns många fler interaktioner som är delaktiga i processen, exempelvis joniska interaktioner och vätebindningar. Den slutgiltiga strukturen av de självaggregerande molekylerna bestäms genom en dragkamp mellan dessa interaktioner.

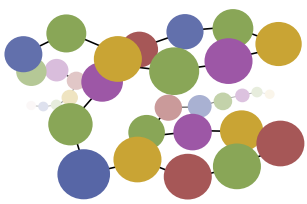

Ett protein

En grupp molekyler som visar ett mångfacetterat självaggregeringsbeteende är proteiner. Dessa är livsviktiga i den mänskliga kroppen eftersom de utför biokemiska processer, utgör stora delar av cellernas transportsystem och också ger strukturellt stöd så att cellerna inte kollapsar. Proteiner är uppbyggda olika byggstenar (aminosyror) och kan liknas vid ett pärlhalsband, där de olika aminosyrorna har specifika egenskaper. Totalt finns det 20 stycken olika aminosyror som används som byggstenar till proteiner och dessa kan vara hydrofoba eller hydrofila, laddade eller oladdade och stora eller små. Exakt hur proteiner självaggregerar beror inte bara på vilka aminosyror proteinet är uppbyggt av, utan även i vilken ordning de sitter.

Att studera hela proteiner kan vara klurigt då de ofta består av flera hundra aminosyror. Istället kan man välja ut en liten del av proteinet och endast analysera den. En sådan kortare kedja av aminosyror brukar kallas en peptid. I den här avhandlingen har vi studerat självaggregeringen i vatten och andra lösningsmedel för modellpeptiderna

A_nK. Peptiderna består av n stycken av den hydrofoba aminosyran alanin (A) och en lysin (K) som kan vara antingen laddad eller oladdad. Det har tidigare visats att de kortare A_6K-peptiderna bildar ihåliga tuber genom självaggregering. De längre A_8K och $A_{10}K$ bilder istället fibrer.

Genom att utnyttja röntgenspridning och elektronmikroskopi har vi kunnat belysa nya detaljer av de självaggregerade strukturerna från A_nK-peptiderna. Vi har exempelvis sett att peptiderna är ordnade på samma sätt oavsett struktur, och att de aggregerade fibrerna är snurrade som ett utsträckt snurrat band. Utifrån dessa fynd har vi kunnat bygga en enkel termodynamisk modell som beskriver de olika bidragen till strukturernas fria energi. Med hjälp av modellen har vi sedan kvalitativt lyckats förklara grundläggande frågor som varför fibrerna är just fibrer, samt varför de kortare peptiderna föredrar att ordnas i tuber istället för i fibrer.

I en annan studie har vi undersökt de gelliknande materialen som bildas när man överstiger en viss mängd A_nK-fibrer. När långa molekylära fibrer blandas i vatten kan dessa nämligen trassla ihop sig vilket i sin tur kan leda till att lösningen blir trögflytande eller ibland bildar geler. Geler som bildats från fibrer i lösning brukar kallas hydrogeler eftersom innehållet av fibrer i förhållande till mängden vatten är försvinnande liten, ibland mindre än 1 : 100. Med hjälp av reologi har vi kunnat se att gelernas styvhet visar ett synnerligen starkt beroende på mängden peptid som använts, betydligt starkare än andra hydrogeler från självaggregerande peptider. Anledningen är att fibrerna i sig är styva, vilket är en effekt av den täta peptidpackningen.

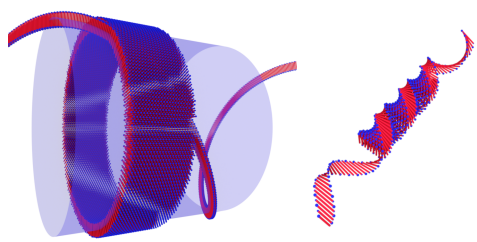

En tub och en fiber av A_nK.

Sammanfattningsvis kan man säga att A_nK-peptiderna har visat sig vara ett intressant självaggregerande modellsystem. Peptidernas enkla uppbyggnad har gjort det möjligt att kunna koppla specifika resultat med systemets specifika egenskaper. Förhoppningsvis kan våra slutsatser vara till nytta för de som studerar mer komplexa system och att de på sikt ska kunna ge en utökad grundläggande förståelse för biologiska processer och inom materialvetenskapen.

List of Publications

This thesis is based on the following publications, referred to by their Roman numerals:

I **Twisted Ribbon Aggregates in a Model Peptide System**

A. Rüter, S. Kuczera, D.J. Pochan, U. Olsson
Langmuir **2019**, 35, 5802-5808

II **Two dimensional oblique molecular packing within a model peptide ribbon aggregate**

S. Kuczera, **A. Rüter**, K. Roger, U. Olsson
Accepted ChemPhysChem **2020**

III **Tube to ribbon transition in a self-assembling peptide model system**

A. Rüter, S. Kuczera, J. Stenhammar, T. Zinn, T. Narayanan, U. Olsson
Manuscript

IV **Self-assembly of model amphiphilic peptides in non-aqueous solvents: changing driving forces, same structures?**

A. Del Guidice, **A. Rüter**, N. V. Pavel, L. Galantini, U. Olsson
Manuscript

V **An isothermal titration calorimetry study of peptide self-assembly**

M. K. Hamid, **A. Rüter**, S. Kuczera, U. Olsson
Manuscript

VI **Slow kinetics in a model peptide system**

A. Rüter, U. Olsson
Manuscript

VII **Arrested dynamics in a model peptide hydrogel system**

A. Rüter, S. Kuczera, L. Gentile, U. Olsson
Submitted Soft Matter **2019**

Author Contributions

Paper I: Twisted Ribbon Aggregates in a Model Peptide System

AR performed all the experimental work and discussed and performed the theoretical work together with SK and UO. AR wrote the manuscript with input from the co-authors.

Paper II: Two dimensional oblique molecular packing within a model peptide ribbon aggregate

SK, UO and AR designed the study and interpreted the data. SK performed the experimental work and wrote the manuscript with input from the co-authors.

Paper III: Tube to ribbon transition in a self-assembling peptide model system

AR, SK, TN and TZ performed the experimental work and data analysis. AR SK and UO designed the theoretical work together with JS. AR wrote the manuscript with input from the co-authors.

Paper IV: Self-assembly of model amphiphilic peptides in non-aqueous solvents: changing driving forces, same structures?

Experiments and data analysis was performed by ADG with assistance from AR. ADG wrote the manuscript with input from the co-authors.

Paper V: An isothermal titration calorimetry study of peptide self-assembly

MKH performed the experimental work supervised by AR and SK. MKH and AR performed the data analysis. UO wrote the manuscript with input from the co-authors.

Paper VI: Slow kinetics in a model peptide system

AR performed the experimental work and data analysis. AR wrote the manuscript with input from the co-authors.

Paper VII: Arrested dynamics in a model peptide hydrogel system

AR performed all the experimental work. AR wrote the manuscript with input from the co-authors.

Abbreviations

CD	circular dichroism
cryo-TEM	cryogenic TEM
D_2O	deuterium oxide/heavy water
DLS	dynamic light scattering
DMF	N,N-dimethylformamide
ITC	isothermal titration calorimetry
LS	light scattering
LVR	linear viscoelastic regime
MeOH	methanol
MSZ	metastable zone
NCC	nanocrystalline cellulose
NMR	nuclear magnetic resonance
SAXS	small angle X-ray scattering
SLD	scattering length density
SLS	static light scattering
TEM	transmission electron microscopy
TFA	trifluoroacetate
WAXS	wide angle X-ray scattering

Prologue

The aim of this thesis has been to characterize the physiochemical properties of a self-assembling model peptide system, the A_nK peptides. These peptides form either tubular or ribbon-like β-sheet aggregates in aqueous solution. Increased fundamental understanding of peptide self-assembly can facilitate the research to find novel biomaterials, to develop new medical treatments using peptide therapeutics and to increase the knowledge of biological phenomena such as amyloidosis, present in diseases such as Alzheimer's, Parkinsons and diabetes type II.

The five most important results and observations are:

- A simple thermodynamic model explains the observed tube to ribbon transition with increasing the peptide length.
- We have detected very slow kinetics of both assembly and dissolution of peptide aggregates, and propose that this a general property of β-sheet systems.
- Fibrillar peptide aggregates from the A_8K and $A_{10}K$ systems can be classified as stiff, sticky and repulsive rods.
- The protonation state of peptides may not necessarily be the same in aggregates as for monomers in solution.
- Even in solvents where the hydrophic effect is weaker, A_nK forms self-assembled structures due to an enhancement of hydrogen bond formation.

1 Introduction

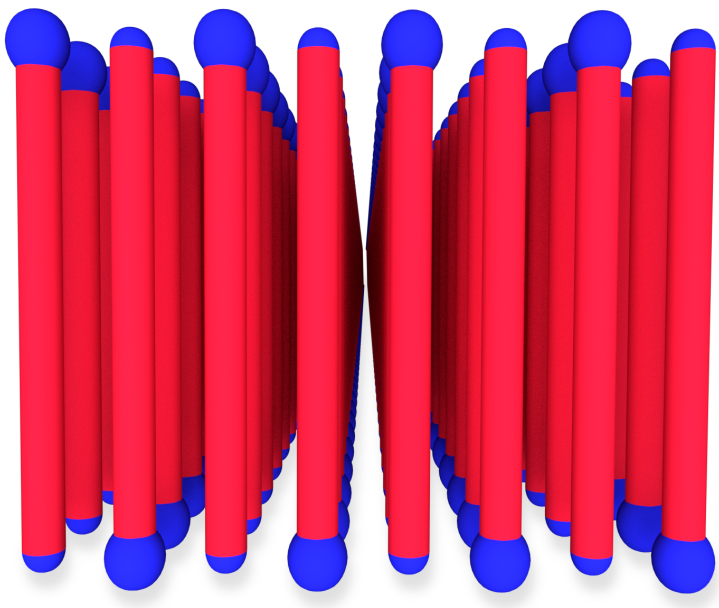

Self-assembly is the process when many small molecules or particles of the same kind spontaneously aggregate and form larger ordered structures.[1,2] It is a common bottom-up procedure for the construction of various structures in nature. Examples include incredible materials such as spider silk,[3] cell membranes[4] and DNA double helices.[5] Self-assembly is also involved in the progress of several severe diseases such as Alzheimer's and Parkinson's, where proteins self-assemble into long fibrillar aggregates that lack function and eventually leads to cell death.[6] The motivation of studying self-assembling systems, is to get a better understanding of relevant biological phenomena.

In this work we have focused on the self-assembly of peptides. This group of self-assembling molecules is particularly interesting not only for the understanding of the mechanisms behind certain biological processes, but also for the potential use in materials science. Self-assembling structures, that are made of biological molecules, are promising and already used for example in various tissue regeneration applications.[7] Another important field of interest is that of peptide therapeutics. Due to the sometimes therapeutic effect of peptides, they are of interest to develop for future therapeutic needs.[8] For success in that area fundamental knowledge of peptide self-assembly is crucial.

1.1 Amino acids, peptides, proteins

Proteins are one of the most abundant macromolecules in the human body, and life without them would simply not be possible.[9,10] They provide structural integrity to the cells, they can form channels to transport cargo across various membranes, and they can control and accelerate chemical processes. Although proteins have this wide variety of tasks, they are all constructed in the same way, as a linear chain of the same building blocks: amino acids. It is the properties of these building blocks and in what sequence they occur that governs the function, size and other properties of the protein. Whereas long chains of amino acids ($>$ 50 amino acid residues) are called proteins, shorter chains ($<$ 50 residues) are referred to as peptides.

There are 20 different amino acids found in proteins that are directly coded from DNA. In the center of the amino acids is a carbon atom, the C^{α}. Connected to the C^{α} is an amine group (-NH_2), a carboxylic acid group (-COOH), a single proton (-H) and a side group R, Fig. 1.1. Every amino acid has a different side group which also governs the general properties of the amino acid. Typical properties that are of interest are if the amino acids are hydrophobic or hydrophilic and if they carry a charge or not. The amino acids of interest for the work presented in this thesis and their properties are presented in Table 1.1. The most simple side group, a single proton, is found in

glycine (G), the only non-chiral amino acid.

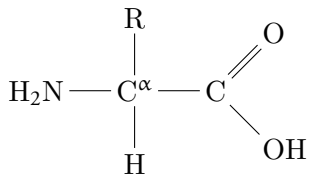

Figure 1.1 An amino Acid

The amino acids are further linked to each other by the creation of a peptide bond through a condensation reaction between the carboxylic acid of one amino acid with the amino group of another. In this way the peptide chain continues to extend to its final length. The final amino acid chain will have two ends. On one side, an amino group, called the N-terminus, and on the other, a carboxylic acid, referred to as the C-terminus. The chain of alternating peptide bonds and carbons is often referred to as the peptide backbone, in contrast to the side groups, denoted R in Fig. 1.1. The repeat distance between peptide bonds in the chain is 3.6 Å.

Table 1.1 One letter codes and main side group property of the amino acids mentioned or worked with in this thesis.

One letter code	Amino acid name	Side group property
G	Glycine	Hydrophobic
A	Alanine	
F	Phenylalanine	
V	Valine	
L	Leucine	
P	Proline	
K	Lysine	Charged
E	Glutamic acid	
S	Serine	Polar, uncharged

1.2 Peptide self-assembly and thermodynamics

Due to the large possible variation in properties of amino acids, peptides are almost always amphiphilic,[11] *i.e.* containing both hydrophilic and hydrophobic components. They may therefore spontaneously self-assemble into ordered structures. The driving force behind this assembly is the hydrophobic effect.[4]

Although the main driving force for the self-assembly is the hydrophobic effect, many other long- and short-range forces are typically involved in the process, such as elec-

trostatic interactions, hydrogen bonding, $\pi - \pi$ stacking and many more.[12,13] Owing to the high presence of carbonyl and secondary amines in the peptide backbones, hydrogen bonding plays a specifically large role in the specific packing of peptides. Through these backbone hydrogen bonds, peptides can form high level of ordering, not possible for ordinary surfactants.

These higher order structures are referred to as secondary structural motifs. In the α-helical structure, the peptide sequence follows a helical path and forms a hydrogen bond with itself every 3.6 amino acid. If instead the peptide strand binds to a second peptide strand and a third and so on, where the hydrogen bonds run perpendicular to the strands, this is called a β-sheet. β-sheets can either be parallel, where all the peptide strands have the C- and the N-termini pointing in the same direction. If the direction instead is alternating, the structure is called anti-parallel. An α-helix and an anti-parallel β-sheet are shown schematically in Fig. 1.2

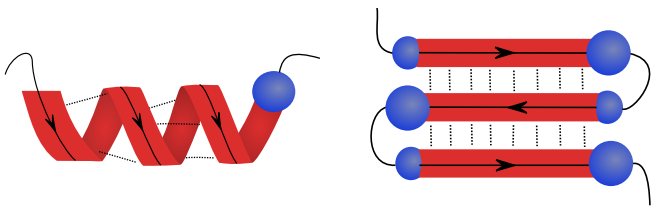

Figure 1.2 A schematic representation of an α-helix (left) and an anti-parallel β-sheet (right). Solid lines and arrows indicate the direction of the peptide backbone. Dashed lines indicate hydrogen bonds. The blue sphere indicates the presence of a hydrophilic amino acid, whereas the red ribbon indicates a stretch of multiple hydrophobic amino acids in a row.

One of the main goals when designing self-assembled materials is to control the mechanism and if possible predict the self-assembled structure. This is a challenge both for experimentalists and theoreticians due to the high level of complexity of peptide sequences: large amino acid sequence variability and a potpourri of intermolecular interactions in the assembled aggregates.[14] A common approach is to study simple peptide model systems from which the fundamental principles can easily be deduced.

1.3 Self-assembling peptide systems

Nature is full of peptides or proteins that self-assemble into hierarchical macromolecular structures.[15] In the early 1990's, Shuguang Zhang decided to have a closer look at a peptide containing a sequence found in regular bakers yeast. He had previously simulated this peptide's interactions and expected it to aggregate into an α-helical structure. Instead he found, that the peptide formed β-sheets and further assembled

into fiber-like structures.[16] The sequence AEAEAKAKAEAEAKA, later referred to as EAK16, showed an interesting structure where one side of the chain consisted of alternating charged peptides and the opposite side was hydrophobic.[17]

Other studied peptide sequences were found in the human body. As part of the transmembrane IsK protein, a 24 residue sequence was found to assemble into fibers.[18,19] The peptide sequence, denoted K24, formed β-sheets that would further laminate. Similar structures of laminated β-sheets had been found in amyloid plaques of patients suffering from diseases such as Alzheimer's, Parkinson's and diabetes type II.[20] Later, a specific seven residue sequence (KLVFFAE) in the Aβ protein, involved in the fibril formation in Alzheimer's disease, was found to form amyloid fibrils on its own.[21,22]

A great deal of work has gone into the formulation of guidelines for the design of self-assembling model peptide sequences.[23,24] A similar pattern as that in EAK16 was used for the fibril forming RADA16 sequence and its variants.[25] The DN1 peptide,[18] and the MAX1 peptide and its derivatives are further examples of designed peptide sequences.[26,27] In the MAX peptide series a central tetrapeptide, -VPPT-, is included to induce a β-turn structure, leading to a hairpin structure of the final protein, that further forms β-sheet fibers.[26] Due to the specific sequence, this turn is pH sensitive and the hairpin structure and the following assembly can be switched on and off. Further derivatives such as the MAX3 has been made thermoresponsive.[27]

Other design principles include the use of α-helical structures for the controlled formation of highly ordered structures[28-30] and $\pi - \pi$ stacking.[31,32] For a general overview of the topic you are directed to some of the following reviews.[15,33-36]

1.3.1 The A_nK model peptide family

In the work presented in this thesis we have studied the self-assembly behavior of the A_nK peptide family. The peptide consists of n alanine (A) residues from the n-terminus and a single lysine (L) amino acid at the c-terminal end. The sequence was introduced in the early 21st century by Zhang and coworkers within the idea of amphiphilic peptides, that are similar to surfactants.[37,38]

A schematic of the A_nK peptide is shown in Fig. 1.3. When uncapped, the peptide has a total of three ionizable groups: both termini as well as the side group of the lysine. At neutral pH or below the peptide will carry a net positive charge, illustrated by the blue color. Due to the hydrophobicity of alanine, most of the peptide is hydrophobic, illustrated by the red color. The peptides are water soluble with a solubility, c_s, that decreases roughly an order of magnitude per added n.[39]

Figure 1.3 A schematic of an A_nK peptide where the main part of the peptide body is colored red due to the hydrophobic properties of the alanine amino acids. The larger blue sphere represents the C-terminus. The ends are colored blue due to the hydrophilic properties.

The self-assembly behavior of the A_nK peptides has to some extent already been elucidated.[39-41] Whereas the shorter A_6K peptides self-assemble into hollow tubes, the longer A_8K and $A_{10}K$ instead assemble into ribbon structures. We want to stress that we in this work mainly use the term *ribbon* to describe the fiber-like aggregates formed from the A_8K and the $A_{10}K$ peptides due to the rectangular cross-section. Elsewhere in literature, the same entity is usually referred to as a fibril or a fiber and a ribbon is often defined as a β-sheet pair, *e.g.* in the theoretical work by Nyrkova and coworkers.[42,43]

1.3.2 This thesis

The aim of this thesis is to expand the understanding of peptide self-assembly. This is achieved by systematic studies of the peptide model system A_nK, which was just introduced. The main focus lies on the ribbon forming A_8K and $A_{10}K$, but to tie our results together with previous work we also show the results form comparative studies with the shorter A_6K peptide. For a holistic view of the system, the experimental work includes studies both on many different length scales and on different time scales. Wherever possible, the experimental work is further compared to existing theoretical work within the field. The results have been divided into three parts, presented in Chapters 3-5.

In the first of these chapters, we revisit the self-assembly structures of A_nK peptide aggregates in aqueous solutions. We conduct a thermodynamic analysis to explain the effect of peptide length on the self-assembled structures from the A_nK sequence. Why do the shorter peptides assemble into tubes whereas the longer prefer a ribbon structure? What are the fundamental energy contributions that contribute to the finite width of the self-assembled ribbons from the A_8K and $A_{10}K$ peptides? We also take a short excursion into the assembly of the A_8K and $A_{10}K$ peptides in non-aqueous solvents. What are the effects on the aggregated structures when the process takes place in a less hydrophilic environment?

In Chapter 4 we turn to the assembly mechanism of the peptide ribbons formed from the A_8K and $A_{10}K$ peptides. We touch upon the question: Are the formed aggreg-

ates equilibrium structures or rather the precipitation of a solid phase? We further characterize the kinetics of the self-assembly and the reverse, aggregate dissolution.

Finally, in Chapter 5, we consider the colloidal aspects of the A_8K and $A_{10}K$ ribbons. Geometrically anisotropic particles can undergo a glass transition at rather low concentrations due to the high excluded volume of elongated objects. This is associated with a dynamic arrest of rotational degrees of freedom. By the addition of salt the predominant interactions of the system changes from repulsive to attractive resulting in a stronger but heterogeneous network rather described as an attractive gel.[44]

2 Methods

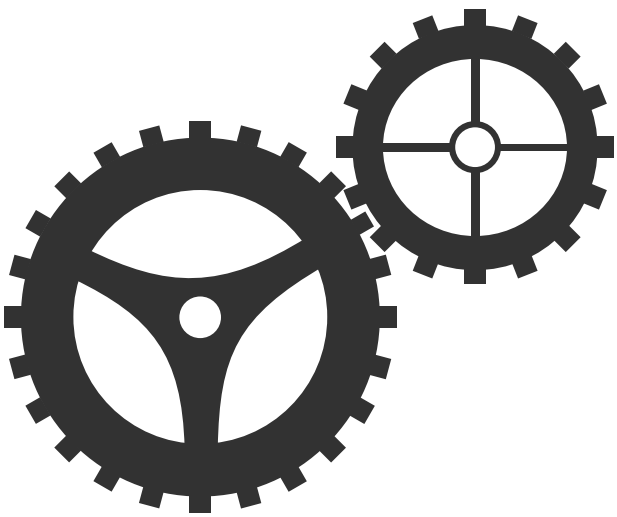

In this chapter I will present a brief general overview of the techniques used in the work behind this thesis. The idea is to give a general introduction to each technique and to introduce the terminology and important notations. I will, at varying level, also introduce ways of analyzing data without by any means recreating a textbook. The varying level of explanations for the different techniques is to some extent a reflection of the respective importance of those techniques during the thesis work.

2.1 Static scattering

Scattering techniques are widely used to characterize soft matter systems.[45-47] The scattering experiments rely on the physical principle of scattering, where the trajectory of an incoming source of radiation is deflected due to the interaction with the atomic components of a sample in its path. If the scattering is elastic, which means that no energy exchange takes place, and the deflected beam is detected before it can undergo a second scattering event, the scattered intensity can be used to gather information about the object that scattered, for example the internal and external structure, dynamics as well as its collective behavior. The radiation either consists of photons such as X-rays or is based on neutron particles. The difference between the types lies in the specific interactions between the radiation and the sample, which can give different experimental benefits. In this work we mainly consider scattering by the means of X-rays, but the underlying theory is the same regardless of the radiation type.

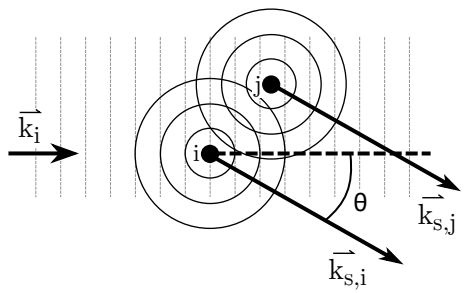

Figure 2.1 An incoming beam described by the wave vector $\bar{k}_i$ is scattered at two point scatterers denoted *i* and *j*. The scattering points emit circular waves described by a wave vector $\bar{k}_{s,ij}$. The amplitude of the resulting varies as a function of the angle with respect to the incoming radiation, θ, due to constructive and destructive interference of the scattered waves.

In Figure 2.1 we consider the scattering of two point scatterers denoted i and j. An incoming electromagnetic wave described by the wave vector $\bar{k}_i$, with the magnitude $|\bar{k}_i| = 2\pi/\lambda$, will be scattered in each of the scattering elements. The result is a spherical wave with the wave vector magnitude $|\bar{k}_s|$. As long as the scattering is elastic, which we assume throughout the text, we have $|\bar{k}_i| = |\bar{k}_s|$. However, their spatial off-

set, $\bar{r}$, gives rise to a phase difference. This difference will give rise to constructive and destructive interference of the waves and therefore the wave amplitudes will depend on the scattering angle θ. To determine this phase separation the scattering vector $\bar{q}$ is defined as $\bar{q} \equiv \bar{k_i} - \bar{k_s}$. Since the scattering event is assumed to be elastic, the magnitude of the scattering vector $|\bar{q}|$, often written as simply q, is determined by

$$q = \frac{4\pi}{\lambda_0} \sin(\theta/2) \tag{2.1}$$

where λ_0 is the wavelength of the incoming radiation. Due to the elastic nature of the scattering event, the scattering vector is the momentum transfer of the event.

The scattering amplitude for the two scattering points is determined by

$$A_S(q) = b_i b_j e^{-i\bar{q}\bar{r}_{ij}} \tag{2.2}$$

where $\bar{r}_{ij}$ corresponds to the spatial vector from scattering point i to j and b_i and b_j are their respective scattering lengths. The scattering length b is essentially a measure of how strong an object scatters. For X-rays, the scattering length depends on the electron density of the specific atom. Unfortunately, the amplitude of an electromagnetic wave is not an accessible parameter from experiments. Instead, the scattering intensity is the product of the amplitude and its complex conjugate, $I(q) = AA^* = |A|^2$. Due to the inability to measure the amplitudes of electromagnetic waves, important information is systematically lost, a caveat of any scattering or diffraction technique referred to as *the phase problem*. As a result, it is essentially impossible to unambiguously determine the structure or the scatterers without *a priori* knowledge.

In a real X-ray scattering experiment atoms are the scatterers and we need to consider many more than two of them. Furthermore, these scatterers will be grouped together to form molecules or particles. For simplicity the particles are assumed to have a homogeneous scattering length density (SLD), ρ, over the whole volume V of each of the scattering objects in the particle, $\rho = b/V$. The function describing the intensity arising from all the scattering point distances within these particles is called the form factor, $P(q)$. Usually a sample also contains a large amount of particles. If interactions occur between the particles, the scattering intensity could also be affected by this. The term describing these interactions is called the structure factor, $S(q)$. We end up with a general version of the scattering equation.

$$I(q) = \phi_p \Delta\rho^2 \langle V_p \rangle \langle P(q) \rangle S(q) \tag{2.3}$$

where ϕ_p is the particle volume fraction, V_p is the volume of the particle and $\langle P(q) \rangle$ is the orientational average of the form factor. At low enough concentrations, or un-

der conditions where interactions are vanishingly weak, $S(q) \rightarrow 1$, meaning that the inter-particle contributions to the scattering can be neglected. $\Delta\rho$, which is the SLD difference between the particle and the solvent, is often referred to as the contrast in scattering. To distinguish the particles from their background, which for biological particles often is water, a large enough difference in SLD is needed between the particles and the background. As the scattering length scales with the electron density, the higher the atomic number the higher the scattering. In the case of light scattering (LS) the interaction also takes place between the incoming radiation and electrons. In this case the electric field, $\bar{E}(t)$, induces fluctuating dipoles in the polarizable molecules.

One of the main concepts of scattering is the notion of reciprocality or *inverse space*. Due to the definition of the scattering vector q as the difference between the incoming and the scattered wave vectors, Eq. 2.1, q will have similar properties as a wave vector, $q = 2\pi/d$, where d is a real space distance. This inverse relationship between q and real space is not only useful to determine what length scale a feature in the scattering curve corresponds to, but it is also conceptually crucial for scattering as a whole. By measuring samples at small values of q, corresponding to small angles, larger features of the sample are observed, whereas at larger q-values, corresponding to larger angles, smaller features are revealed. This is also reflected on a practical level as X-ray scattering measurements are divided into small and wide angle scattering, SAXS and WAXS. Reaching certain angle regimes is achieved by changing the distance between the detector and the sample.

2.1.1 Data analysis

Analyzing scattering data can be done in many different ways. Generally, a distinction is made between model independent or model dependent approaches. The model independent methods are calculations based on scattering theory and the calculations do not rely on any a-priori assumptions or input parameters. Accessible values are for example the radius of gyration, molecular weight or a general size estimate of a certain feature. In the model dependent approach different theoretical models are tested against the experimentally obtained scattering data. This can deepen the knowledge of the system by giving information on the size and shape of the particles, if they are monodisperse and if they interact with one another in a specific way.

First of all we come back to the notion of reciprocality. We saw that we can relate a certain q-value to a real space distance d. As we know from theory, the intensity at a certain q-value depends on the occurrence of that distance in the sample. If that occurrence is high it will give rise to a peak in the scattering pattern. The q-value of the peak can be related to an inter-particle distance as in an ordered colloidal crystal, or

the spacing between layers in a lamellar stack, or it can be related to an intraparticle distance, *e.g.* crystal planes in a particle. To estimate that distance one simply uses $d = 2\pi/q$.

At low enough q-values, approximately $qR_G < 1$, details of the particle form factor will no longer affect the scattering signal. Instead the signal can be approximated to only depend on the zero angle scattering, I_0, and the radius of gyration of the particle, R_G. This is referred to as the Guinier approximation and the scattered intensity, $I(q)$, is given by

$$I(q) = I_0 e^{\frac{-(qR_G)^2}{3}} \tag{2.4}$$

By plotting $ln(I(q)$ as a function of q^2 it is possible to extract R_G from a scattering experiment. We can also extract molecular weight information from $I(0)$, in dilute solutions where $S(q) \approx 1$, and thus Eq. 2.3 can be rewritten as $I(q \to 0) = cM_w\Delta\rho^2/N_A\rho^2$, where c is the aggregate concentration, M_w is the weight averaged aggregate molecular weight and ρ is the peptide density.

Often the model-independent analysis can be complemented with models to gain an even better knowledge of the system of interest. For example the scattering data can be modeled to the theoretical form factors of well-defined geometries. For simple geometries it is possible to analytically calculate their $P(q)$ as shown in Eq. 2.3.[48] The $P(q)$ for spheres, cylinders and discs are shown in Figure 2.2, and a list of roughly 40 different $P(q)$ can be found in Ref[48] or in the Sasview software.[49] At low enough q-values, all of the shown geometries show a q independent scattering. Furthermore, we see that the scattering at the high q-limit for the shown geometries shows a q^{-4} dependence. In between however, there are differences depending on the spacial distribution of mass in the particles. For a cylinder, where the mass is distributed along one dimension, the scattering at these dimensions should scale as q^{-1}. For a plate, where the mass is distributed in two dimensions in the intermediate q-regime, $I(q) \propto q^{-2}$.

Analytic expressions of $S(q)$ are known only for a few model cases.[48] These are generally valid for particles of spherical symmetry and spherical interactions. It is however possible to experimentally determine an effective $S(q)$.[50] In the low concentration regime, the experimental form factor can be determined as $P(q) = I(q)/\phi\Delta\rho^2\langle V_p\rangle$. By normalizing a scattering curve at a higher concentration with the experimental form factor, it is possible to determine an effective structure factor $S_{eff}(q) = I(q)/P(q)$. This is often enough to give a quantitative estimate of the interactions present and quantitative information on characteristic length scales in the sample.

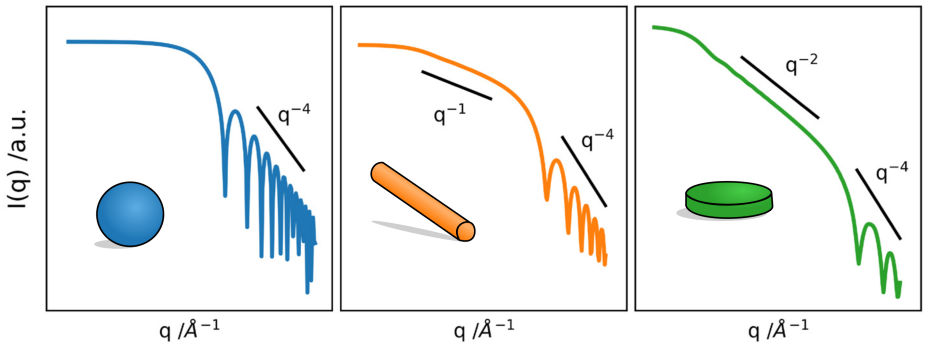

Figure 2.2 Theoretical scattering form factors for spherical, rod and disc shaped particles. The characteristic slopes associated with the specific shapes are shown.

2.2 Dynamic scattering

A snapshot of a 2D scattering pattern from a sample undergoing Brownian diffusion reveals what is referred to as a *speckle pattern*. Due to the interference of the scattered waves, the intensity fluctuates in all directions on the detector. Due to the diffusion of the particles in the sample, the speckles will fluctuate with a certain speed related to the particle mobility. At high dilution this is given by the Stokes-Einstein relation

$$D = \frac{k_B T}{6\pi\eta R_H} \tag{2.5}$$

where D is a diffusion coefficient, k_B is Boltzmann's constant, T is the absolute temperature, η is the viscosity of the solvent and R_H is the so-called hydrodynamic radius.

In order to determine the diffusion coefficient, an intensity auto-correlation function is measured. The intensity over a certain time is recorded at very small time intervals, usually in the nanosecond range. The correlation of the intensities is calculated by multiplying the intensity at every time point $t + t_0$ with the intensity at the starting point t_0. At early time points, the intensity pattern has not had time to change much and the intensity will be highly correlated with that at t_0. Over time, the correlation is completely lost. By normalizing the whole signal with the squared average intensity one acquires the so called normalized intensity auto-correlation function

$$g^{(2)}(q,\tau) = 1 + \beta \left(g^{(1)}(q,\tau) \right)^2 \tag{2.6}$$

where β is an instrumental constant and $g^{(1)}(q,\tau)$ is the normalized time auto-correlation function of the electromagnetic field, which is non-measurable quantity.

Instead $g^{(2)}(q,\tau)$ is the measured correlation function of the intensity. Eq. 2.6 is often referred to as the Siegert relation[51].

In a dilute sample of perfectly monodisperse spherical particles, where particle interactions can be neglected, the decay of the correlation function follows a monoexponential decay, with a decay time $\tau_c = 1/q^2 D$. If the particles are polydisperse the field correlation function consists of a sum of exponentials. One way of extracting the diffusion coefficient was introduced by Koppel in the early 1970s[52] and is referred to as the *method of cumulants* where the field correlation function is assumed as

$$g^{(1)}(\tau) \equiv \int_0^\infty P(\Gamma)\, e^{-\Gamma\tau}\, d\Gamma \tag{2.7}$$

where $P(D)$ is a weight factor of every exponential with decay rate $\Gamma = -q^2 D$, q is as always the scattering vector and $\int P(\Gamma)\, d\Gamma = 1$. The exponential is linearalized and Eq. 2.7 is rewritten to

$$\ln\left(g^{(1)}\right) = -\bar{\Gamma}\tau + \frac{1}{2}\left(\frac{\bar{\Gamma^2} - \bar{\Gamma}^2}{\bar{\Gamma}^2}\right)\left(\bar{\Gamma}\tau\right)^2 + \ldots \tag{2.8}$$

introducing the so called Z-averaged decay rate, $\bar{\Gamma}$. The second term in Eq. 2.8 is used to determine the distribution of decay rates, which corresponds to the polydispersity of the spherical particles in solution.[53]

2.3 Rheology

Rheology is the science of flow and deformation of matter.[54,55] The term is often used to describe the experimental method of rheometry. In this thesis we are dealing with the rheology of what is known as *soft matter*, which is a collective term for materials with structures on a length scale from 1 nm to 1 μm where thermal fluctuations play a significant role. They are of special interest since they are viscoelastic, which means that they show both viscous properties and elastic properties.

The typical rheological measurement involves shear flow and can be visualized by two plates between which a sample is placed, Figure 2.3. The bottom plate is stationary and to the top plate a shear force, F, is applied parallel to the stationary plate. The resulting shear stress, σ is defined as $\sigma = F/A$, where A is the area of the plates. The force results in a deformation, or a strain, $\gamma = \Delta x/l$ to the sample, where Δx is the distance the top plate has moved and l the distance between the plates. The stress and

the strain of an elastic material are related through the shear modulus G in Hooke's law as $\sigma = G\gamma$. The stress in a liquid follows Newton's law instead, *i.e.* $\sigma = \eta\dot{\gamma}$, where η is the viscosity and $\dot{\gamma}$ is the shear rate. There are two main measurement types in rheology. Either the sample is subjected to a continuous shear or the deformation is varied in an oscillatory fashion, with a certain amplitude and frequency.

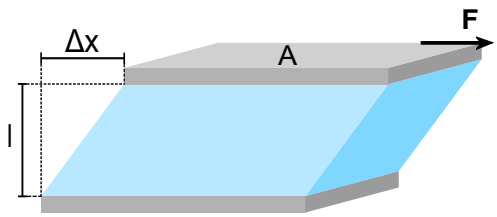

Figure 2.3 A schematic image of a rheological experiment. A force F is applied on the top plate with area A, parallel to the bottom. As a result, the sample of thickness l is displaced by Δx

In the general example of the rheological measurement in Fig. 2.3, a sample is shown between two parallel plates. That specific measurement setup is referred to as *parallel plates*. In the *cone plate* geometry the top plate is exchanged with a downward facing truncated cone. This allows for a constant shear rate, $\dot{\gamma}$, throughout the whole sample volume, which is not the case in the parallel plate geometry. The cone plate geometry is the one used in the work presented in this thesis.

2.3.1 Continuous shear rheology

Continuous shear rheology is used to characterize the flow properties of the material, *i.e.* the stress, σ, or the viscosity, η, as a function of the shear rate, $\dot{\gamma}$. This can for example be a good method to simulate how the material reacts if it is applied using a syringe. The parameters are, as previously mentioned, related through Newton's law. How easily a material flows is determined on a molecular scale. It is a measure of how easily the molecules in the solution can slip past each other. For large rough particles that easily get stuck on one another, the viscosity will generally be high. High viscosities can also be reached at rather low sample concentrations if the particles in solution are long 1D objects, since these easily entangle and form a transient network.

If the viscosity of a material is independent of $\dot{\gamma}$, it is referred to as a Newtonian material. Water is an example of a Newtonian liquid. Soft matter materials however are typically non-Newtonian. This shows up as a non-linear behavior in the measured shear stress or a viscosity, that varies with $\dot{\gamma}$. If the viscosity decreases with $\dot{\gamma}$, the material is shear-thinning, and vice versa. Ketchup is a good example of a shear-

thinning material. As the bottle opening is much smaller, the shear rates are much higher. The resulting flow of the ketchup is a result of shear-thinning.

Self-assembled peptide hydrogels are typically shear-thinning[56,57]. The shear-thinning mechanisms for this behavior can however vary. In a system of stiff rods, the shear can induce an alignment of the rods along the flow, which reduces the viscosity. However, if the rods are very long and have many crossing points, a high shear might also lead to rupture of the network and of the individual fibers. Usually, it is beneficial to use a complementary measurement technique, such as LS or SAXS/WAXS, to gain further information. It is also possible to combine rheology with polarized light microscopy, as the induction of particle alignment will give rise to birefringence.

As the networks in hydrogels are often connected through physical interactions rather than chemical bonds, the structures are to some extent self-healing. This means that the hydrogel can recover its strength after a certain amount of time. For many applications this can be an interesting property. In that case the constant shear measurement is followed by an oscillatory measurement to track the dynamic behavior as a function of time after cessation of flow.

2.3.2 Oscillatory shear rheology

In oscillatory rheology the shear stress is applied in an oscillatory sinusoidal fashion. The applied stress is characterized by an strain amplitude, γ, and an angular frequency, ω. The resulting stress or strain is measured and can reveal if the probed material is predominantly viscous or elastic.

If the material is purely viscous, the resulting strain is in phase with the applied stress. If the material on the other hand is elastic, the resulting strain has been phase shifted 90° to the applied stress. The relation between the stress and the strain for oscillatory measurements is related through the complex or dynamic modulus $G^* = \sigma/\gamma$. The complex modulus gives the phase shift of the signal and the response is given in terms of the storage modulus G', containing the elastic component, and the loss modulus G'', containing the viscous component, $G^* = G' + iG''$.

The generalization of Hooke's law, with G^*, holds for small deformations, where the viscoelastic response is linear, or in the so called linear viscoelastic regime (LVR). The border of this regime can be determined through a measurement where the amplitude of the oscillations are varied and is defined as the regime where G' and G'' are constant. In the LVR, G^* and its components are often determined as a function of the frequency. The oscillatory shear measurements probe if the system has enough time to recover from the applied stress before an opposing stress is applied. If the

stress relaxation time, τ, is shorter than the inverse of the applied frequency, ω^{-1}, the sample behaves as a liquid under these time-scales and $G' < G''$. If, on the other hand, $\tau > \omega^{-1}$, which implies that $G' > G''$ and the sample predominantly behaves as an elastic solid. If the frequency and the relaxation time are inversely equal, *i.e.* $\omega = 1/\tau$, we have the cross-over point where $G' = G''$. Many materials have several degrees of freedom, each with different τ.

2.4 Nuclear magnetic resonance

Atomic nuclei can posses what is called a nuclear *spin*, which will give rise to what is known as a magnetic moment.[58] This is the case when the sum of protons and neutrons in the nucleus is odd or if the amount of protons and neutrons are both odd, for example in ^{1}H or in ^{13}C. In a sample the spins of the atomic nuclei are randomly oriented, but when subjected to an external magnetic field, $\bar{B}_0$, they will align either with or against $\bar{B}_0$. These two states (spin up or spin down) have a slightly different energy, ΔE. The exact value of ΔE depends on the chemical surrounding of the nucleus. In nuclear magnetic resonance (NMR) spectroscopy this difference in ΔE can be utilized to differentiate between the same atomic nuclei within a single molecule.

To detect ΔE in an NMR measurement, a weak oscillating magnetic field with a frequency, ν, is applied over the sample. The frequency is related to energy through the relation $E = h\nu$, where h is Planck's constant. If the frequency matches ΔE we achieve what is referred to as resonance, and the energy will be absorbed. By detecting the absorbed frequencies, we can track the content of a sample. The integral of an acquired spectrum is directly proportional to the concentration of that specific nucleus type. The signal from NMR is therefore quantitative as long as the intensity can be calibrated[59].

NMR spectra are generally present on a *chemical shift* scale, where the frequency is presented as a frequency shift away from a reference frequency. The unit of the shift is parts per million. A proton NMR spectrum of an $A_{10}K$ sample is shown in Fig. 2.4.

The linewidth of the NMR spectrum is defined by the rotational dynamics of the sample constituents. For solid samples the tumbling is slow resulting in a very broad linewidth. Individual molecules on the other hand tumble around freely and the resulting linewidth is small. In Fig. 2.4, the observed resonances only occur from freely dissolved peptide monomers and the signal from the solid aggregates has such a broad linewidth that it is inseparable from the background.

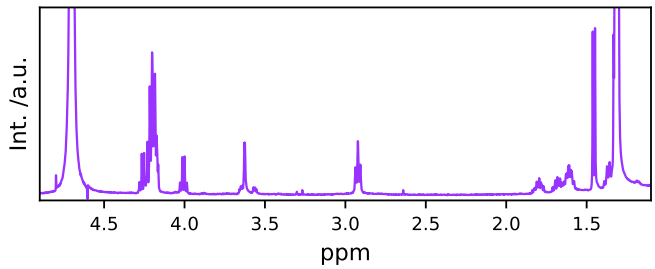

Figure 2.4 A proton NMR spectrum of $A_{10}K$ with a total peptide concentration approximately 1 mM. The resonance at roughly 2.9 ppm arises from the protons in one of the -CH_2 groups in the lysine side group.

2.5 Isothermal titration calorimetry

Calorimetry is a technique used to determine the change in heat that takes place during a specific chemical or physical process.[60] From this heat the enthalpy of the specific change can be determined. A specific calorimeter sub-type is the isothermal titration calorimeter (ITC). In ITC one gradually titrates one solution into another. In our case, we have studied the process of dilution titrating a highly concentrated solution into a lower concentration or pure solvent. This is specifically interesting for studying the phase transitions in self-assembling systems.[61,62]

A typical ITC consists of a reference cell and a sample cell that are kept at the same temperature. A needle is connected to the sample cell into which another liquid can be injected. In our experiments, we considered the process of peptide aggregate dissolution. A highly concentrated solution of peptides is therefore titrated step-wise into the pure solvent. If the resulting sample cell concentration is below the peptide solubility, c_s, the aggregates will dissolve, resulting in a change in temperature of the system. The temperature change is matched in the reference cell, and the power needed to do so, ΔP, is monitored. If the process in the sample cell leads to a temperature increase, the transition is called *exothermic*. If the sample cell temperature instead decreases due to the process, it is referred to as *endothermic*.

The signal from an ITC measurement can consist of simultaneously occurring processes. For example when a highly concentrated sample of self-assembled molecules is injected into pure solvent, we will need to consider both dilution and dissolution of the aggregates[61]. Once all contributions are correctly separated, they can be further analyzed. The main goal of an ITC measurement is typically to determine thermodynamic parameters such as the change in enthalpy, ΔH.

2.6 Transmission electron microscopy

In regular optical microscopy the resolution limit is determined by the wavelength of the visible light and the dimensions of the aperture, generally known as the *Abbe limit*. Visible light has wavelengths in the range of hundreds of nanometers and is therefore not capable of visualizing objects on the nanometer scale. With the introduction of the particle-wave duality of the electron came the idea of using electrons for imaging.[63] The electron has a wavelength on the order of sub-nanometers, which makes the imaging of nanometer sized structures possible. Since then electron microscopy has undergone significant improvements and nowadays electron microscopes have the ability to resolve sub-atomic structures.[64]

In the typical transmission electron microscope (TEM) an electron beam is generated and accelerated towards the sample. Unlike in optical microscopy, it is not possible to use regular glass optics to focus the light. Instead the beam is focused using magnetic lenses. As the beam hits the sample, some electrons are scattered or diffracted, whereas some pass straight through. Further lenses are used to recreate and enlarge a 2D image of the sample.[65]

As with any imaging technique, contrast is an important concept. Since biological materials seldom are crystalline, the contrast of the sample in TEM is defined by the ability to scatter electrons, *i.e.* material contrast scales with atomic number. This makes the analysis of biological material difficult as these are high in chemical compounds with a rather low atomic number, such as carbon, hydrogen, oxygen and nitrogen. The contrast is further diminished as the sample is usually placed on a grid coated with a carbon film. To resolve this issue of low contrast, it is possible to stain the samples by introducing a high molecular weight salt such as phosphotungstic acid or uranyl actetate[66]. The increased amount of high atomic number components will give rise to an increased electron scattering and therefore also contrast. In bright field TEM this type of staining is referred to as *negative*, as it inverts the intensities and the samples appears bright on a dark background. Unfortunately, the introduction of further components to the system can strongly alter the sample in a non-predictable way.[67]

A second issue arises in the study of biological samples during a standard TEM measurement. Small biological specimen are often present in solution, where they diffuse freely. To image such particles, they need to be fixated, which can be achieved by either substituting the water for a suitable resin or by drying. In either case the solution conditions: ionic strength, pH, hydrogen bonding propensity *etc.* is difficult or impossible to keep constant. This can not only lead to collapsed supramolecular structures, but also to concentration induced phenomena such as assembly/disassembly of

equilibrium structures or aggregation.

The issue of sample fixation was solved by the introduction of cryogenic TEM (cryo-TEM)[68]. It has been considered a major breakthrough in the characterization of biological samples. In this technique, a liquid sample is placed on a sample grid with small holes where the solution is suspended. The grid is vitrified, *i.e.* frozen without the introduction of ice crystals, by cryogenic freezing. This step is necessary, since the diffraction from ice crystals will cover the weak signal from the sample. The measurement then takes place on the sample in the frozen state. Images taken using cryo-TEM are considered to better represent the sample in the solution state, and due to an incredible development in the field of electron optics the last decades, cryo-TEM can now even be used for crystal structure determination of for example proteins.

In Fig. 2.5 a schematic comparison is made between the introduced sample preparation techniques. The illustration highlights the main benefits and drawbacks of the various sample preparation techniques. Both negative staining and cryo-TEM have major benefits over the regular sample preparation technique of drying. However, while the stained sample has a lot higher contrast due to the high molecular weight salt, the solution structure might still not be retained, and possibly even altered. In cryo-TEM, on the other hand, the solution structure of the sample is believed to be retained to a large extent and although the contrast is not as good as when using staining the main drawback of the technique is the difficulty of sample preparation. Not only does the preparation of cryo-TEM samples require extra instrumentation but also highly skilled and patient technicians.

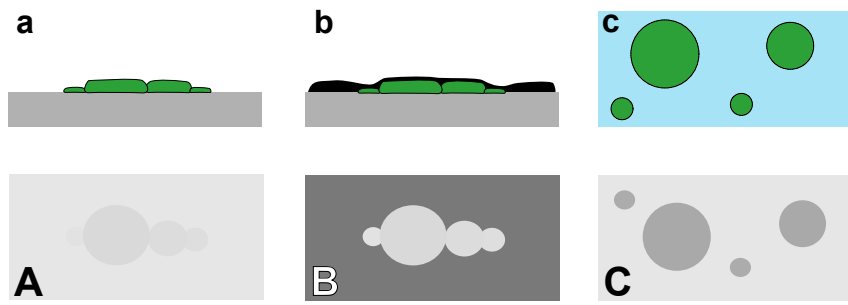

Figure 2.5 A schematic of three different sample conditions in TEM with their respective resulting 2D image. (A) Biological samples give poor contrast in regular dry TEM samples, where the sample has been fixated on a carbon film. Furthermore, one cannot be sure that the sample integrity is maintained, ***e.g.*** otherwise spherical vesicles might collapse and aggregate. (B) Through a negative stain the contrast issue can be resolved. However, the sample integrity can still be a problem. Furthermore, the introduction of a high molecular weight salt can also introduce other artifacts. (C) In cryo-TEM the contrast is usually lower as compared to using a negative stain. on the other hand this sample preparation method is best in retaining the actual conditions of a sample in solution.

2.7 Circular dichroism

Circular dichroism (CD) is a non-destructive spectroscopic technique which can detect chiral species in solution.[69,70] One of the most common uses of the technique is to determine the secondary structure of proteins. Secondary structural motifs such as α-helices or β-sheets will, due to their specific chiral structures, give rise to fingerprint spectra. The main features of these spectra are found in the UV regime.

In CD the sample is illuminated by circularly polarized light which contains both left and right circularly polarized components of the same magnitude. If the sample only contains non-chiral molecules in solution, the magnitude of the two components will still be equal after passing through the sample. A sample containing chiral molecules on the other hand, will show a preferential absorption of one of these components, giving rise to a a magnitude difference of the two components at the detector. The difference in the polarization is measured and presented as a function of the wavelength of the incoming light. Approximations of typical fingerprint spectra from the most common secondary structural motifs are shown in Fig. 2.6.

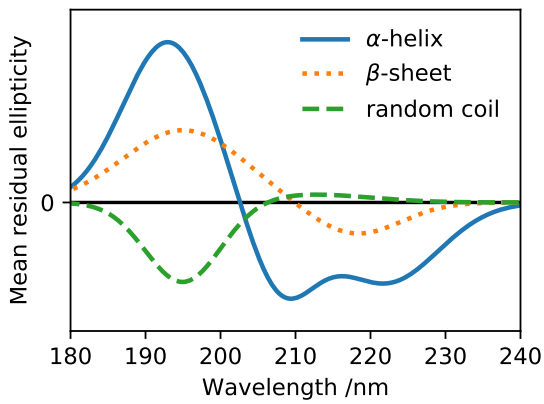

Figure 2.6 Approximations of the fingerprint CD spectra from secondary structure units of proteins.

The analysis of CD data can be difficult as the measured signal is a linear combination of the spectra arising from all the different entities in the sample. For unknown protein systems, the acquired spectrum can be compared to various databases containing CD spectra of proteins where the full protein structure has been verified by other techniques. This has shown to be rather useful for full length protein systems, however, when it comes to the analysis of short model peptide systems, the results can be misleading as to what structures are actually present.[71]

In this work, CD has mainly been used as a proof of β-sheet formation, and therefor as a detector for peptide aggregation. When peptides are dissolved in solution as free peptide monomers, their CD signal will mostly resemble that of a random coil. If instead aggregation occurs and the formed aggregate shows some other secondary structural unit, the signal would instead show a specific secondary structure signal. The technique is therefore useful in order to probe the aggregation as a function of concentration, time, pH or temperature.

3 Structure & Thermodynamics

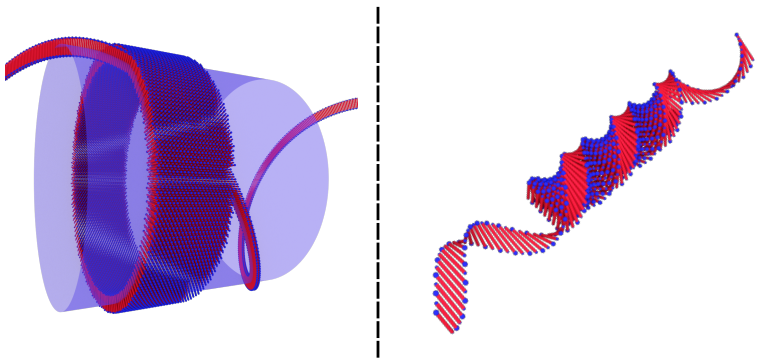

The starting point of understanding the basics of peptide self-assembly is to acquire a detailed perception of what the self-assembled structures look like. Due to the fact that most self-assembled structures from peptides have geometries on the nanometer length scales, ordinary optical microscopy is not applicable. Instead, scattering techniques are often used. The self-assembled structures of the A_nK peptides, where $n = 6, 8, 10$, have previously been investigated using both scattering techniques and electron microscopy,[39-41,72,73] showing that the shorter A_6K peptides form hollow nanotubes and A_8K and $A_{10}K$ peptides form ribbons.

In this chapter we have revisited this structural characterization. From high quality data we have been able to lay down the last pieces of the puzzle concerning the structural characterization of A_nK aggregates. From this we have devised a simple thermodynamic model which aims to explain some of the main questions regarding the structures: why the A_8K and $A_{10}K$ ribbons seem to have a constant width, and why the shorter A_6K peptides prefer to assemble into tubular structures rather than ribbons. Furthermore, we have studied the self-assembly of the longer A_nK peptides in non-aqueous solvent. The results presented in this chapter are based on Papers I-IV.

3.1 Aqueous self-assembly

To highlight the strikingly different self-assembly behavior of the shorter and the longer A_nK peptides, SAXS and WAXS patterns of A_nK ($n = 6, 8, 10$) are shown in Fig. 3.1. In Fig. 3.1A, the higher concentration of A_6K shows a scattering intensity consisting of well-resolved features in both the high and the low q regime in contrast to the lower concentration. These features indicate the presence of self-assembled structures. For the A_8K and the $A_{10}K$ peptides we also observed a scattering intensity that is varying with q, and again the observed features in both the high and the low q regime tells us that self-assembly has occurred.

For a better idea of the assembled structures, the scattering curves are compared to the theoretical scattering curves of various shapes and geometries. The lower A_6K concentration, $\phi = 0.07$, shows a scattering pattern consistent with that of a random coil with $R_G = 5.5$ Å.[48] This is in line with what has been estimated previously.[72]

Based on previous work on the A_6K system we know that the peptides self-assemble into tubular structures.[40,41,72] From Fig 3.1A it becomes clear, that the sample contains a large fraction of freely dissolved peptide monomers. The scattering pattern of the higher concentration is therefore compared to a linear combination of the Gaussian coil model and a hollow tube model.[48] The model reveals parameters such as the tube wall thickness, 3.3 nm, previously not accessible in scattering experiments,

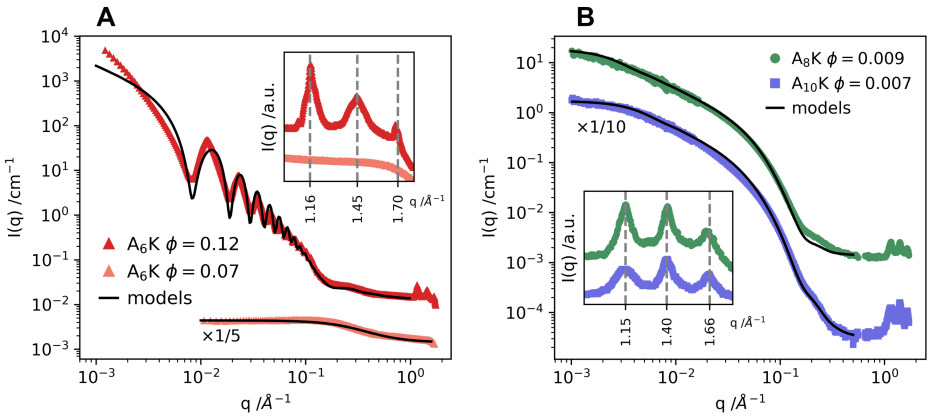

Figure 3.1 SAXS and WAXS curves of A_nK ($n = 6, 8, 10$) together with theoretical models describing the macromolecular structure. (A) The scattering curve of A_6K shows the characteristic scattering pattern of a hollow tube with the core radius 27.5 nm, the tube wall thickness 3.3 nm and a 4 % polydispersity. As the peptide solubility, ϕ_{sol}, is high, the model compared to the experimental data of A_6K, $\phi = 0.12$ contains a non-interacting contribution from a dispersion of monomeric Gaussian polymer coils with $R_G = 5.5$ Å, successfully describing the solubilized peptide volume fraction. (B) The scattering curves of A_8K and $A_{10}K$. Both these peptides self-assemble into 1D objects and the scattering patterns are compared to the theoretical scattering of an elliptical cylinder with semiaxes $a = 1.9$ nm and $b = 3.8$ nm, and an average length of $\langle L_{A8K} \rangle \approx 180$ nm and $\langle L_{A10K} \rangle \approx 100$ nm. A polydispersity of 15 % is included in the model for A_8K and 20 % for $A_{10}K$. Scaling factors have been applied for data in both panels to enhance visibility.

although suggested based on solid state NMR measurements.[74] The polydispersity is low, 4 %. An explanation for this strikingly low polydispersity is presented later in this chapter. Finally we note a discrepancy between the data and the model in the low q regime, most likely due to a structure factor contribution.

The self-assembled structures of the A_8K and $A_{10}K$ are best modeled as elliptical cylinders.[39,75] In Fig. 3.1B we observe the Guinier regime for both peptide systems from which we can estimate the average aggregate length, $\langle L \rangle_{A8K} \approx 180$ nm and $\langle L \rangle_{A10K} \approx 100$ nm. For A_8K we observe a small discrepancy between the model and the data at $q \approx 0.2$ Å^{-1}, which we ascribe to a small contribution from the solubilized free peptide monomers, that is higher than the peptide solubility, which will be further presented in Chapter 4.

Both self-assembled structures in the A_nK system show three distinct Bragg reflections in the WAXS regime, which indicates a high degree of local peptide ordering. Moreover, both structures have been shown to give rise to a strong β-sheet signal using techniques to determine the peptide secondary structure.[39,73] Based on the structural data, the aggregates from the studied peptides consist of monolayers of laminated β-sheets. The ordering is limited to two dimensions. For the A_8K and $A_{10}K$ assemblies,

this implies a rectangular cross-section.

We propose a local peptide packing in a two-dimensional (2D) oblique lattice with the unit cell shown in Fig. 3.2, for both the tube and the ribbons. The unit cell parameter a corresponds to the direction of the β-sheet. From such a unit cell the three first Bragg reflections observed in the WAXS regime would correspond to the 01, $2\bar{1}$ and 20 reflections of the unit cell.

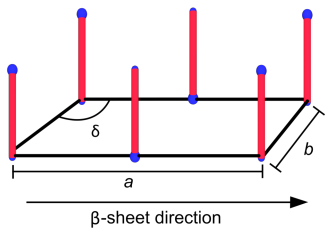

Figure 3.2 An oblique unit cell with the parameters $a \neq b$ and $\delta \neq 120$. The β-sheet direction is parallel to a and due to the anti-parallel β-sheet configuration $a = 2d_0$, where d_0 is the peptide-peptide distance within a β-sheet.

To further verify the proposed unit cell in the A_8K and $A_{10}K$ ribbons, we performed WAXS experiments on aligned peptide aggregates.[76] The alignment locks the orientational degrees of freedom of the aggregate and it is then possible to determine the orientation of the crystal lattice within them. Acquired 2D WAXS patterns for aligned samples of A_6K and $A_{10}K$ are shown in Fig. 3.3. In both cases, the propagation axis of the structures are roughly aligned with q_x. The angle, φ, between the 01 reflection and the average propagation axis of the aggregate reveals the β-sheet orientation in the aggregates. In the tubes this angle has previously been determined to $\varphi = 52°$,[73] indicating that the β-sheets run on a helical path around the tube. For the $A_{10}K$ ribbons we observed $\varphi = 90°$, indicating that the β-sheets run parallel to the ribbon axis.

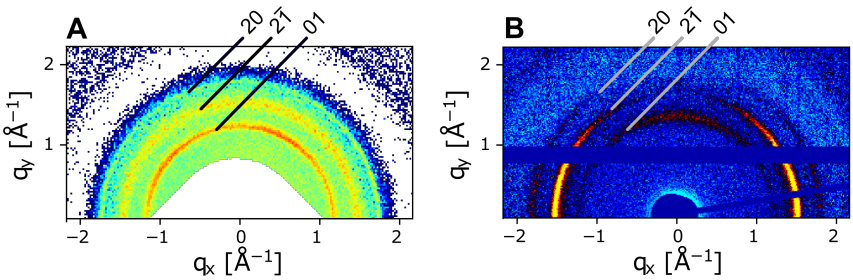

Figure 3.3 2D WAXS patterns of the (A) A_6K and (B) $A_{10}K$ peptide systems where the average propagation axis of the aggregates are oriented roughly along q_x. The anisotropy shows that the peptide packing within the tubes is crystalline.

That $\varphi \neq 90, 0$ for the A_6K tubes has great implications on the geometry. Due to the crystalline lattice and its specific helical pitch angle, the contour length of the helical pitch, λ_c, must fit an integer multiple of the lattice parameter a, Fig. 3.4. The same

goes for the pitch, λ_t, which must fit an integer multiple of the lattice parameter b. These restrictions highly limit the available combinations of φ, λ_c and λ_t, which in turn only allow a very specific tube radius. This phenomenon is also found in other systems forming self-assembled tubes of a low polydispersity and of a high level of 2D ordering.[77-80]

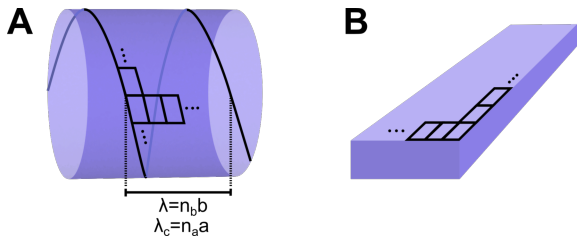

Figure 3.4 A schematic showing how the oblique crystal unit cell is oriented in the tube (A) and in the ribbon (B). In the tube both the pitch length, λ, and the contour length of the helical path, λ_c, must be integer multiples of the lattice parameters b and a respectively. This constrains the dimensions of the tube explaining the experimentally acquired low polydispersity

The ribbon structure, as determined by SAXS/WAXS measurements for A_8K and $A_{10}K$, was confirmed using cryo-TEM, Fig. 3.5. Width estimates are in line with the scattering results, but acquiring a reliable estimate of the length was difficult. In areas where individual ribbons were observed, the aggregate lengths were under underestimated. Most likely, the longer ribbons in solution are more likely to entangle with other ribbons and end up in regions where they are visibly difficult to separate. We could however conclude, that both systems have a large length polydispersity.

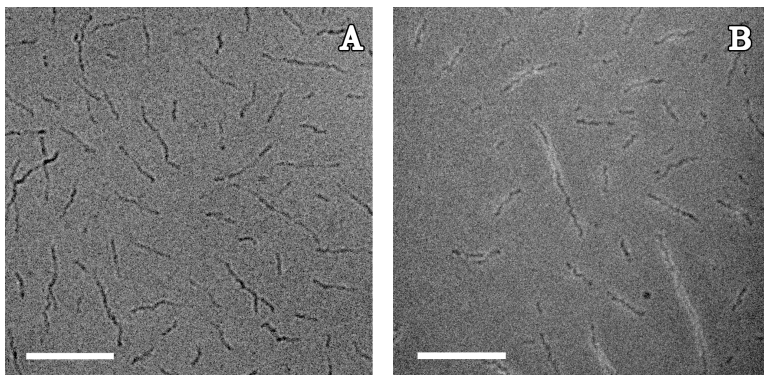

Figure 3.5 Cryo-TEM images of (A) A_8K and (B) $A_{10}K$. The scale bars correspond to 100 nm.

Peptides are chiral molecules and the chirality is typically hierarchically transferred also to the macroscopic structures which they form. Ribbons formed from laminated β-sheets therefore typically show a macroscopical twist with a pitch λ_r around the propagation axis of the fiber,[43,81,82] although non-twisted polymorphs also exist.[83]

In the cryo images, shown in Fig. 3.5, such a twist is not clearly observed. However, when the contrast is increased by negative staining in regular TEM, the twist is clearly appreciable as intensity oscillations along the fiber, Fig. 3.6. The pitch, λ_r, was determined to 16 nm for both peptides. The value of $\lambda_r/w \approx 2$, where $w = 8$ nm is the ribbon width, is low in comparison to other twisting fiber systems.[43,82] This low pitch-width ratio is probably an artifact from the stained and dry TEM samples. Such a short pitch would result in extreme β-sheet deformations, as will be presented below.

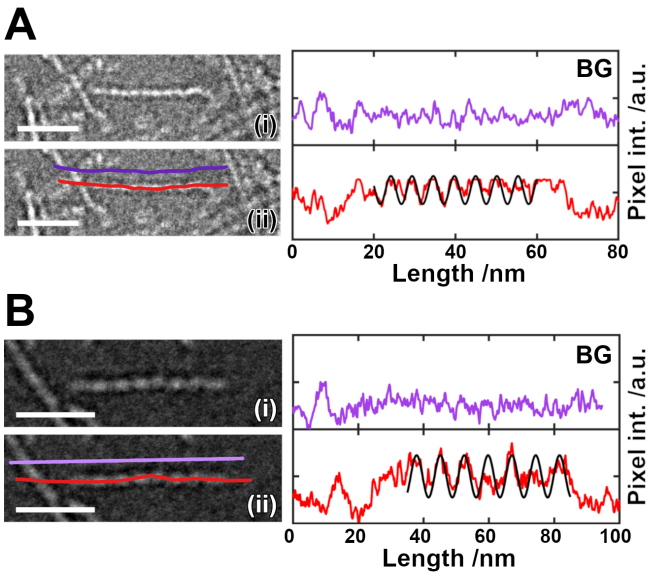

Figure 3.6 Negatively stained TEM images of A_8K and $A_{10}K$ aggregates respectively in A and B. (i) shows the raw image and (ii) shows the same image with two lines indicating the position of the two traces shown. The line trace of the fiber is fitted by eye to a sinusoidal function to extract the pitch of the intensity oscillations. The scale bars correspond to 30 nm.

3.2 Structure models

Both structures observed in the A_nK peptide system consist of laminated anti-parallel β-sheets.[39,76] From the WAXS analysis we determined both the repeat distance between β-sheets, $d_{lam} = 0.54$ nm and the peptide-peptide distance within a β-sheet, $d_0 = 0.45$ nm.[76] The height of the β-sheet is determined by the length of the peptide, $l_p = d_A(n+1)$, where $d_A = 0.36$ Å is the length of an individual amino acid and consequently the distance between hydrogen bonding sites along the peptide length and n is, again, the number of alanine amino acids in the peptide sequence. These

distances are shown schematically in Fig. 3.7. The number of hydrogen bonds in the β-sheets are assumed to correspond to the total number of amino acids, *i.e.* $(n+1)$.

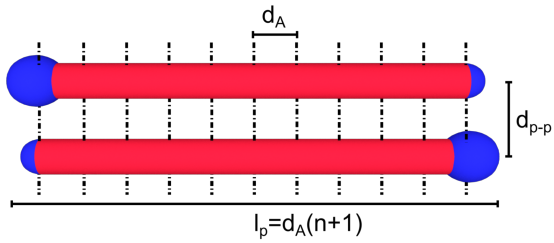

Figure 3.7 A schematic of an A_nK peptide pair within a β-sheet. The peptide length is determined by $l_p = d_A(n+1)$, where d_A is the length of an individual amino acid. The peptide separation in the β-sheet is denoted d_0.

A schematic of the A_6K tubes is shown in Fig. 3.8, where we also show an enlargement of one of the β-sheets. It becomes evident, from the helical path of the β-sheet, that the sheet is subjected to a bending deformation.

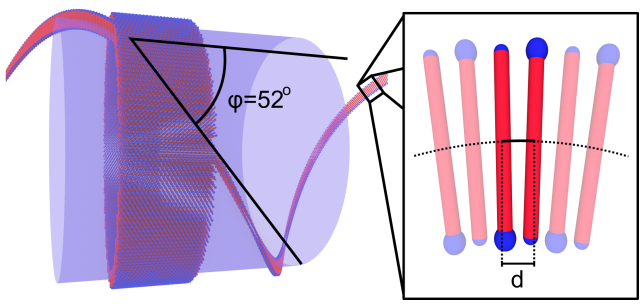

Figure 3.8 A schematic of the tube structure formed by A_6K peptides. The peptides form a monolayer of β-sheets around the tube perimeter where the β-sheets follow a helical path with an pitch angle $\varphi = 52°$. The curvature of the β-sheet path leads to a bending deformation of the sheets.

The twisted ribbons formed in the A_8K and $A_{10}K$ are shown schematically in Fig. 3.9. Due to the chirality of the β-sheets the ribbons twist with a pitch, λ_r. For further discussion we choose do index the β-sheets within the structure symmetrically from the ribbon center. For an odd total number of sheets, the central β-sheet is denoted $m = 0$. The total number of sheets is $N = 2M + 1$, where M is the absolute value of the $m_{\max}$.

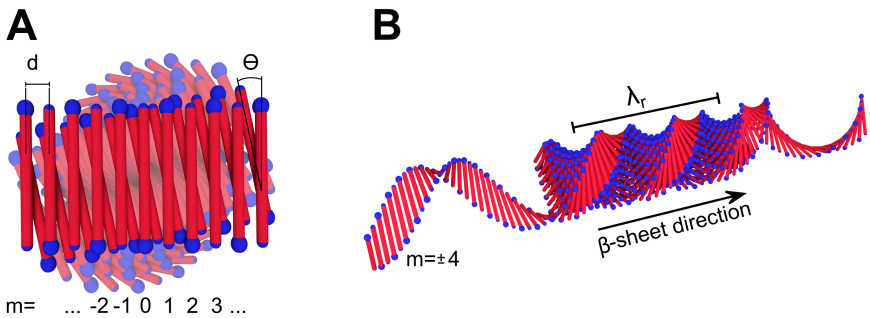

Figure 3.9 A schematic representation of the peptide ribbons in the A_8K and $A_{10}K$ systems. (A) Viewing the ribbon along the axis of propagation. (B) A side view where the outermost β-sheet has been extended showing how the β-sheets $m \neq 0$ lie on a helical path.

From Fig. 3.9B it becomes evident that with increasing $|m|$ the contour length of the β-sheets increases. This leads to an increased extensional deformation of the hydrogen bonds with a corresponding free energy penalty.[42]

3.3 Free energy models

As seen from the structural discussions, the A_nK system consists of two macroscopically rather different structures: tubes and twisted ribbons, which, on the other hand, are very similar in terms of the molecular packing. We have also seen that the β-sheets in the respective structures are subjected to slightly different deformations. Peptide self-assembly is an intricate process where the total energy of the system is determined by a combination of various energy contributions including hydrophobic, electrostatic and van der Waals interactions and hydrogen bonding.[12,83] In order to explain the structural differences in the A_nK peptide system, we have devised a simple thermodynamic model which takes into account various energy contributions in the system. We assume that a sum of these contributions is a valid estimate of the the total free energy of either structure.

The model includes three energy contributions. First, an interfacial energy contribution

$$\mu_{\text{int}} = \frac{\gamma 2(n+1) d_A d_0}{N} \tag{3.1}$$

where γ is an interfacial tension. This contribution accounts for hydrophobic interface area in contact with the solvent. A second contribution is included to account for the elastic deformations of the β-sheets, where the deformation is estimated as a

change in d_0, at the position of the hydrogen bonds, holding the β-sheets together. We assume that this contribution can be described by the harmonic potential

$$\Delta E = \frac{1}{2} k_{\text{def}} (d - d_0)^2 \tag{3.2}$$

where k_{def} is a spring constant and d indicates the peptide-peptide distance in a deformed β-sheet, which can vary along the peptide. The contribution to the chemical potential due to β-sheet deformation, μ_{def}, is given by the sum of all potential energies from each hydrogen bond. Finally we also consider the chirality of peptides by including a contribution arising from the untwisting of the β-sheet structures described by

$$\mu_{\text{twist}} = \frac{1}{2} k_{\text{twist}} (\theta - \theta_0)^2 \tag{3.3}$$

where k_{twist} is an elastic constant and θ_0 is the optimal peptide-peptide angle in radians. θ and the pitch, λ, are related through $\theta = 2\pi d_0/\lambda$.

Based on the proposed contributions to the chemical potential we can derive equations for the full chemical potential of the observed structures in the A_nK system. For the self-assembled peptide tubes we have $\mu_{\text{int}} = 0$, which gives

$$\mu_{\text{tube}} = \mu_{\text{def}} + \mu_{\text{twist}} \tag{3.4}$$

Furthermore, the β-sheets have to be completely untwisted ($\theta = 0$) to fit the proposed structure.

In Paper I we present a simple thermodynamic model for the peptide ribbons, which describes how the twisting of the β-sheets limit the ribbons to a specific width, based on the previous work of Nyrkova et al.[42,43] In Paper III we instead focus on the comparison between the tube and the ribbon free energies and the model from Paper I has therefore been revised on a couple of points. First we note, that μ_{twist} must be present with a significant value due to the presence of the twist in the ribbons. This was not needed in Paper I, as the contribution is constant. Secondly, we have changed to a more general harmonic potential function for the elastic β-sheet deformation. The total energy of the ribbon as presented in Paper III is determined by

$$\mu_{\text{ribbon}} = \mu_{\text{int}} + \mu_{\text{def}} + \mu_{\text{twist}} \tag{3.5}$$

As in Paper I, the model results in an energy minimum for a finite number of β-sheets, N.

With expressions for the total free energy of both structures we could compare the two structures with each other as a function of the total alanine content, Fig. 3.10. The calculations are made with a certain set of parameters presented in Table 3.1. From the set values, γ, k_{def}, k_{twist} and θ_0 we minimize the energy for μ_{ribbon} so that $N = 15$, in agreement with the experimentally determined ribbon width.

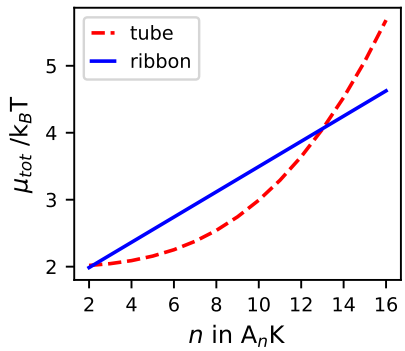

Figure 3.10 The total free energy for both tube and ribbon structures as a function of peptide length. A cross-over in the most favorable structure from tubes to ribbons is found at $n \approx 13$.

For this specific parameter set we see that the model shows a cross-over in energy between the tube and the ribbon configuration. This is in qualitative agreement with the experimental results. However, we seem to overestimate at which peptide length this should occur by roughly a factor of 2, as Fig. 3.10 shows the cross-over at $n \approx 13$. In experiments the transition occurs at $6 < n < 8$.

Table 3.1 Parameters used for the free energy calculations shown in Fig. 3.10.

γ /$k_{\text{B}}T\,\text{nm}^{-2}$	k_{def} /$k_{\text{B}}T\,\text{nm}^{-2}$	k_{twist} /$k_{\text{B}}T\,\text{rad}^{-2}$	θ_0 /rad	λ_{r} /nm
6	1500	100	0.2	90

The calculations are based on a simplified expression for μ_{def}, and we not, that a more detailed estimate would possibly give different results. Furthermore, we do not include any energy contribution from electrostatic interactions as both structures form under the same solvent conditions.

In summary, we have successfully have created a model that predicts a transition from tubular structures to ribbons as a function peptide length. We note, that it would still be possible to further optimize the used parameters to shift the cross-over towards the experimental result, however, the scope of this project has rather been to increase the general understanding of the system. We see, that our model further agrees with other systems forming self-assembled nanotube,[77-80] in the sense that the tubular structure is limited to shorter molecules.

3.4 Non-aqueous assembly

As previously shown, the driving force for self-assembly is the hydrophobic effect and the final structure relies on the competition of various non-covalent molecular forces, where their relative strengths are often governed by the solvent in which they occur. We have therefore investigated the self-assembly behavior of A_8K and $A_{10}K$ peptides in non-aqueous solutions, where the hydrophobic effect is assumed to be weaker.[84] The chosen solvents where methanol (MeOH) and N,N-dimethylformamide (DMF).

Due to the increased hydrophobic environment of both the chosen solvents, we expected the solubility of a hydrophobic peptide to increase. Instead, we observed the opposite. We determined the solubility using SLS on a dilution series of the peptide solutions in the two solvents, Fig. 3.11. The solubility was estimated from the concentration where the signal became indistinguishable from the background scattering. For A_8K we observed a decrease of the solubility by at least a factor of 100. The $A_{10}K$ solubility was found to have roughly the same solubility.

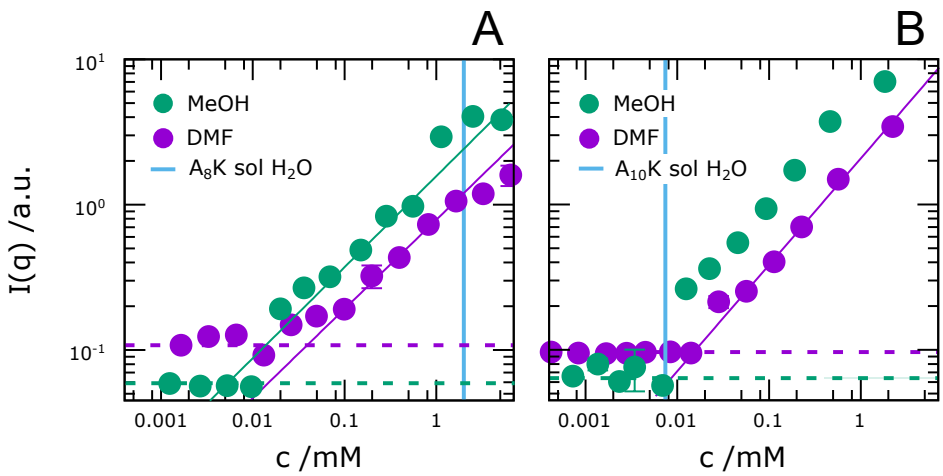

Figure 3.11 Peptide solubility experiments, using SLS, of A_8K (A) and $A_{10}K$ (B) in MeOH and DMF. The horizontal line indicates the peptide solubility in H_2O, and dashed lines represent the background scattering of the respective solvents.

We interpret the lowering of the solubility as an effect of the decreased hydrogen bonding capacity of the solvents. We note, that DMF is only a hydrogen bond acceptor. This will promote the internal hydrogen bond formation in the peptide aggregates as shown by studies of proteins in *e.g.* MeOH.[85] Another contribution to the decrease in monomer solubility should come from the less favorable ion solvation. The overall effect is a lowering of the peptide solubility.

Structural analysis of the assembled structures was carried out using SAXS, Fig. 3.12. In both solvents we observed the same general self-assembly behavior as in water. The SAXS scattering patterns normalized for concentration and SLD all overlap in the intermediate q range. The resemblance of the patterns also in the high q regime indicates, that aggregates are most likely ribbon-like. At low q values however, the data in non-aqueous solvents show a decrease in $I(q)$ as well as a more prominent $S(q)$ peak at approximately $q \approx 0.2$ Å. This indicates that the inter-ribbon interactions are stronger than in water.

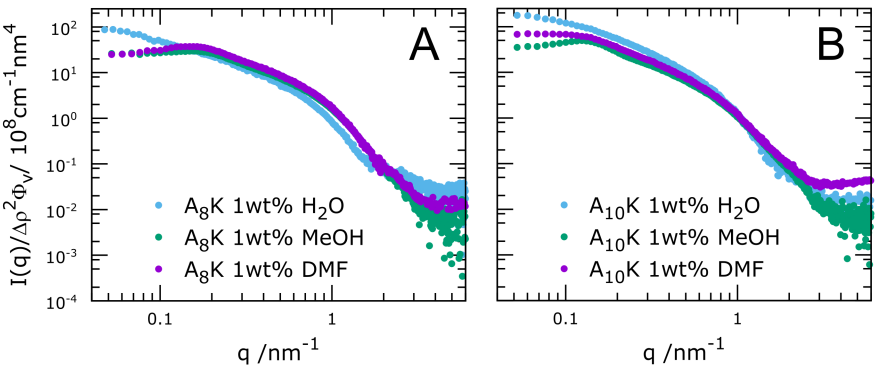

Figure 3.12 Scattering patterns of (A) A_8K and (B) $A_{10}K$ in H_2O, MeOH and DMF. The data is normalized for both SLD and ϕ resulting in an overlapping curves for $q > 0.2$ nm^{-1}.

The ribbon structure was further confirmed from cryo-TEM images, Fig. 3.13. Qualitatively, the aggregated ribbons seem both longer and straighter than when imaged in water. This in agreement with the idea of a lower solubility. As the solubility is lower, more ribbons will be formed. Also the observed increased inter-ribbon interactions are observed as the ribbons in the images are well separated.

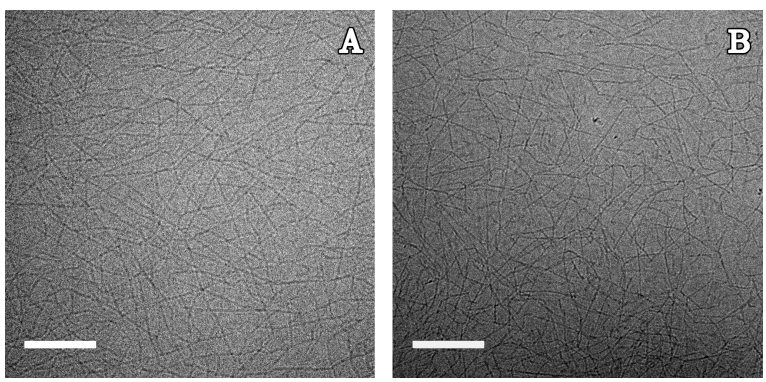

Figure 3.13 Cryo-EM images of (A) A_8K and (B) $A_{10}K$ in MeOH. The scale bars correspond to 100 nm.

The presence of noticeably stronger repulsive interactions is also rather counterintuitive, as electrostatic repulsion typically decreases with the dielectric constant. We assume, that this is described by a combination of effects. First of all, we note, that the lowered solubility for A_8K means a reduction of free monomer in solution. This reduces the ionic strength and, consequently, the screening of the electrostatic repulsion.[4] This would, however, not explain the increased interactions for $A_{10}K$. We must, therefore, also consider the increase in steric excluded volume due to the increased length of the ribbons. This will lead to more overlap at lower concentrations, increasing the osmotic pressure of the solution and effectively lowering $S(0)$.

3.5 Conclusions

In this chapter we revisited the structural determination of the self-assembled aggregates of the A_nK peptides in water. By acquiring new high resolution TEM images we were able to show that the A_8K and $A_{10}K$ peptide ribbons are twisted. This is due to the chirality of the peptide molecules. We have further interpreted the similar WAXS pattern from the non-similar self-assembled structures: tubes and ribbons. From experiments we showed that the peptides in both structures pack on a 2D lattice. This crystalline peptide packing explains the low observed polydispersity of the self-assembled tubes in both A_6K and in similar systems.

Based on the final structural model we could construct a simple thermodynamic model describing the free energies of the two observed structures. The model considers a sum of energy contributions. The first contribution comes from the interfacial energy of available hydrophobic interfacial area in contact with water. The second contribution comes from the elastic deformation of the β-sheets as an affect of adopting a certain structure. The third and final contribution comes from the untwisting of the optimally twisted β-sheets.

The model successfully elucidated why the A_8K and $A_{10}K$ ribbons are limited in width. Furthermore, we qualitatively captured the observed experimental transition from a tube structure from the shorter A_6K peptides, and ribbons for the longer ones. This also fits rather well with the observations from several other studies that tube structures only form from short peptide sequences. In longer sequences and full protein studies, the dominating structure is the β-sheet based ribbon or fiber.

We finally also studied the self-assembly of the A_8K and $A_{10}K$ peptides in the non-aqueous solvents MeOH and DMF. Although the strength of the hydrophobic interaction was decreased, the propensity to form intra-ribbon hydrogen bonds was enhanced. A lowering of the peptide solubility further resulted in the formation of

more and longer ribbons. The overall structure is the same as that found in water, whereas the inter-ribbon interactions are found to be enhanced.

4 Kinetics of assembly and dissolution

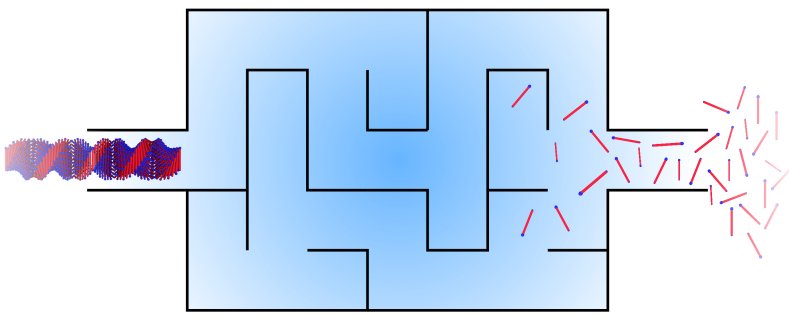

In this chapter, we will present the results from Papers V and VI, where we moved away from the steady state properties of the A_nK self-assembly and focused on resolving the molecular pathway of the process. We have tried to unravel the molecular mechanism of assembly by touching upon the question whether the assembly can be considered an equilibrium state, as for surfactant micelles, or rather as kinetically stable particles. For this characterization, we have mainly used NMR and protein secondary structure characterization techniques. From our studies, we have also been able to characterize the kinetics of assembly.

Further properties of peptide assembly of interest are the mechanisms of dissolution and its kinetics. For this we used ITC, a technique mainly associated with thermodynamic characterization of micellization processes. It is a powerful technique also very useful in peptide self-assembly. Finally, we have also had a closer look at the pH of the solution and how this is affected by the assembly behavior.

4.1 The assembly process

As was shown in Chapter 3, the peptides in the A_nK aggregates are crystalline. Crystals grow through the two-step process of crystallization: nucleation and growth.[86] To study the self-assembly process of the A_nK peptides, we decided to track the free monomer concentration using proton (NMR). A spectrum of the $A_{10}K$ peptides has already been shown in Fig. 2.4, where the resonances arise from the free peptide monomers in solution. Assuming that the peptide monomers in the aggregates have close to zero degrees of freedom, their fast relaxation gives rise to a peak with a linewidth much larger than the studied experimental range. This contribution is therefore inseparable from the background.

To quantify the peptide monomer concentration, c_{mon}, the integral of the resonance at approximately 2.9 ppm was measured against a calibration curve from samples with a known concentrations of tetramethylammonium chloride (TMAC), Fig. 4.1. This resonance was determined to belong to the two protons in the -CH_2 group furthest out on the lysine side group. The exact same acquisition parameters were used throughout all the measurements.

From the calibration measurements, we could determine c_{mon} as a function of time, Fig. 4.2A. We observed a slow decrease of c_{mon}, reaching a steady state concentration, c_∞, after roughly 10 days. Furthermore, $c_\infty \gg c_{\mathrm{s}}$, where c_{s} is the peptide solubility. We define a supersaturation, $\sigma = c_\infty / c_{\mathrm{s}}$, which here has the value ≈ 30.

We notice, that the measured c_{mon} at the first measurement point only corresponds to roughly 20 % of the total peptide concentration. An increased time resolution was

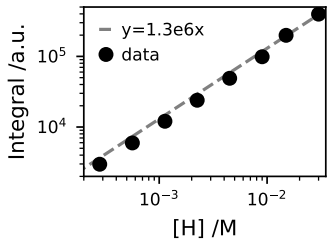

Figure 4.1 A calibration curve for the proton content in an NMR spectrum with the same acquisition parameters as used for the peptide. The calibration curve was produced from samples of known concentrations of TMAC.

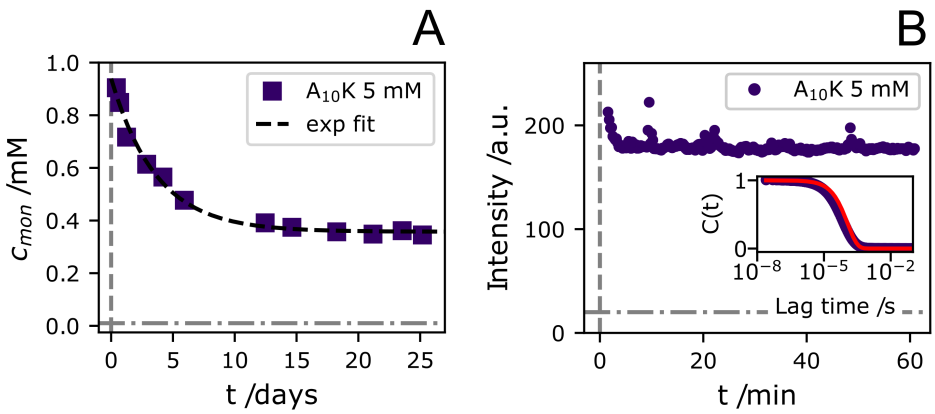

Figure 4.2 (A) The detected c_{mon} in an $A_{10}K$ sample with a starting concentration of $c = 5$ mM. Gray dashed lines show the sample preparation time, $t = 0$ (vertical), and the peptide solubility (horizontal). After roughly 10 days c_{mon} reaches a steady state concentration c_∞ determined by a single exponential fit to the data. (B) Static light scattering of a sample of the same concentration as in (A). Gray dashed lines indicate The preparation time, $t = 0$, (vertical) and the typical solvent scattering intensity from the instrument (horizontal). The insert shows the simultaneously acquired normalized intensity correlation function. Assuming only translational diffusion we estimate $L \approx 40$ nm, using cumulant analysis.

achieved by the means of SLS, where the signal arises from the aggregates rather than the monomers. In Fig. 4.2B, the scattered intensity, $I(q)$, is presented as a function of time, where the first measurement point was acquired 14 s after preparation. The constant intensity, higher than the indicated solvent scattering, shows the presence of larger scattering objects, that do not significantly change size during the experimental time window. From a cumulant analysis of the simultaneously collected correlation function, and assuming that the decay is a result of translational diffusion, we can determine these to peptide aggregates of 40 nm. We conclude, that the nucleation rate is higher than the growth rate.

The reaction rate constant of a process, k, can typically be described by

$$k_+ = k_0 e^{-\Delta E_a / k_B T} \tag{4.1}$$

where k_0 describes the rate at which the correct configuration is probed, and the exponential term describes a probability for the process to occur based on the ratio between its activation energy ΔE_a and the thermal energy. For a diffusion controlled process k_0 is high and ΔE_a is low or non-existing. We note however, that the observed growth kinetics in the $A_{10}K$ system cannot be explained within the timescales of a diffusion controlled process,[87] and must therefore be reaction controlled. The crystal growth of small organic molecules has also been found to be an reaction controlled process,[88] and slow growth rates have further been found in both protein crystallization and in the growth of amyloid fibers.[89-92]

To explain the observed slow growth kinetics, we consider the aggregate growth on a molecular level. The $A_{10}K$ ribbons have been shown to be limited in width,[75] and therefore only grow through peptides attaching at the ends of the laminated β-sheets. The peptides at the β-sheet ends are assumed to form 11 hydrogen bonds to the neighboring peptide and 11 hydrogen bonds to the solvent. For a new peptide to dock to the structure, peptide-solvent hydrogen bonds need to be replace with peptide-peptide hydrogen bonds. Whereas a single hydrogen bond has an energy of roughly $5 - 10$ k_BT, it is possible that multiple hydrogen bonds need to be replaced simultaneously for this process to occur. This would give an activation energy which may very well be on the order of $10 - 20$ k_BT or higher.[93] We further note, that due to the complexity of the molecular pathway of growth, k_0 should also be low. The resulting low value of k_+ is proposed to be a general feature of growth β-sheet containing fibers.

The observed steady state concentration, c_∞, is further found to be independent of c if $c > c_\infty$, Fig. 4.3A. Samples prepared below c_∞ do not show a significant decrease in NMR intensity over time, indicating that no nucleation has taken place. We interpret this as the upper limit of a meta-stable zone (MSZ) for aggregate growth.[88]

To further confirm the absence of nucleation below c_∞, concentrations above and within the MSZ were measured using CD spectroscopy, Fig. 4.3B. These measurements confirm the lack of secondary structural ordering of the peptides below c_∞, whereas above c_∞ the spectrum shows the signature features of β-sheet formation and thus the presence of aggregates.

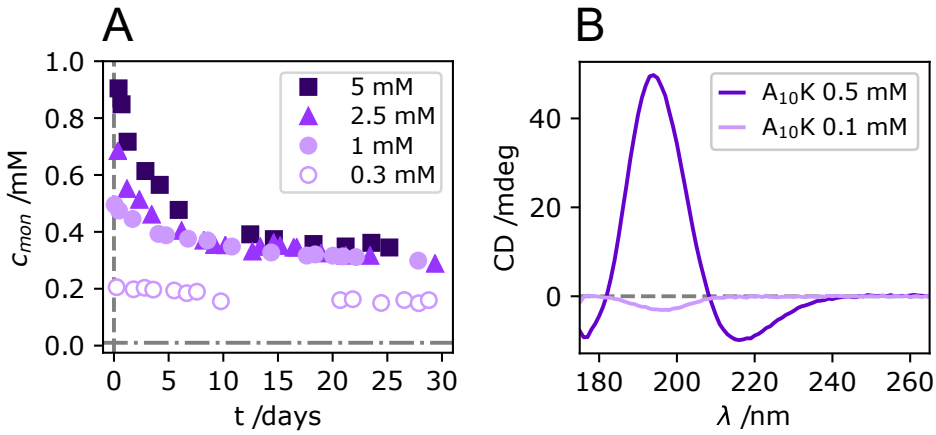

Figure 4.3 (A) c_{mon} over time for four $A_{10}K$ samples with different starting concentrations. Samples above c_∞ all converge to c_∞ whereas the sample prepared at c_∞ only shows a very minor decrease. (B) CD spectra of $A_{10}K$ above and below c_∞.

4.2 Aggregate dissolution

Further thermodynamic characterization of the system was performed using ITC. This technique is commonly used for studying the micellization process,[61,62] rather than to study peptide self-assembly.[94] With the rising interest in the field, the last decade has seen a start of ITC studies of peptide self-assembly.[94-96]

In two ITC experiments, a highly concentrated solution of A_8K was injected into a sample cell containing either pure solvent or a solution already containing A_8K peptides, Fig. 4.4. Every injection increased the total concentration of the measurement cell by roughly 0.21 mM, giving a total concentration range of $0-8$ mM of both the experiments. The majority of the signal is seen to be exothermic, however, small endothermic contributions can also be observed. The data from the two measurements will further be referred to as data sets A and B.

From the ΔP trace, we observed four different processes. These were further distinguished by analysis of their kinetics. The main part of the exothermic process appeared to have a concentration dependent time behavior, expected for the process of aggregate dissolution[97]. The three other processes were instead fast with constant kinetic behavior. We therefore assumed, that all the fast processes could be ascribed to the dilution processes. We considered $\Delta P = \Delta P_{\text{dil}} + \Delta P_{\text{dis}}$. The associated ΔH values of the processes were estimated by $\Delta P = dH/dt$. To estimate ΔH, we modeled the individual processes observed in the ΔP-trace of each injection. We mainly focused on the enthalpy of dissolution, ΔH_{dis}.

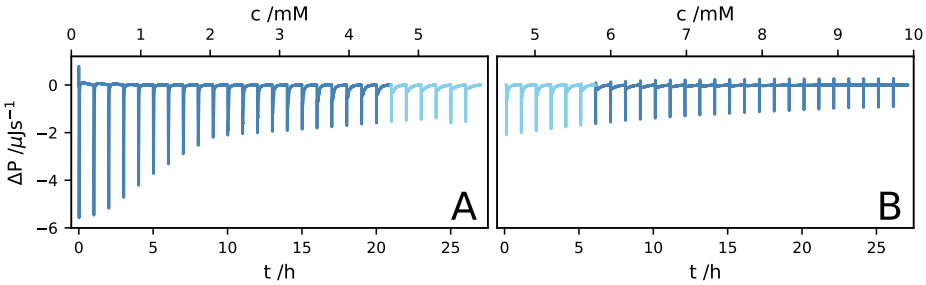

Figure 4.4 The differential power ΔP as a function of time in two ITC experiments of the A_8K system. A 27 mM A_8K solution was serially injected in pure solvent (A) or into a 4.4 mM A_8K solution (B). The last 6 injections of (A) and the first 6 injections of (B) represent a similar concentration range.

A test function for the monomer concentration over time was assumed to be explained by

$$c_{\text{mon}}(t) = c_{\text{mon}}(0) + \left(1 - f_{\text{agg}}\right) \Delta c(t) + f_{\text{agg}} \Delta c(t) \left(1 - e^{-kt}\right)^{\alpha} \tag{4.2}$$

where c_{mon} is the concentration of free peptide monomer at $t = 0$, $c(t)$ is the total peptide concentration at a given t, $\alpha > 1$ represents an effective lag time, f_{agg} is the fraction of aggregates of the injected peptides and k is the rate of dissolution. We assume that $\Delta P \sim dc_{\text{agg}}/dt$. Considering the third term of Eq. 4.2 we reach

$$\Delta P_{\text{dis}} = A f_{\text{agg}} \Delta c_0 \left[k_{\text{inj}} e^{-k_{\text{inj}} t} \left(1 - e^{-kt}\right)^{\alpha} + \left(1 - e^{-k_{\text{inj}} t}\right) \alpha k e^{-kt} \left(1 - e^{-kt}\right)^{\alpha - 1} \right] \tag{4.3}$$

where A is a constant, k_{inj} is a rate constant that describes the increased peptide concentration during the duration of the injection. The change in enthalpy is further given by

$$\Delta H = \int_0^{\infty} \Delta P_{dis} dt = A f_{\text{agg}} \Delta c_0 \tag{4.4}$$

In the modeling of the fast processes, we only sought to capture the features of ΔP as closely as possible, rather than choosing theoretically correct functions. It turned out, that these traces can be sufficiently well described by either half a period of a sinusoidal function or of a Lorentzian distribution. The model functions for ΔP_{dil} and ΔP_{dis} are shown together with the ΔP-traces from four injections in Fig. 4.5. From these graphs we could clearly distinguish the three different processes assumed to be associated with dilution. There are two fast endothermic processes, one occurring only during the first

injections, and one only occurring towards the higher concentrations. An exothermic process also seems to be present. The minimum of this exothermic process coincides with the ending time of the injection, $t = 30$ s.

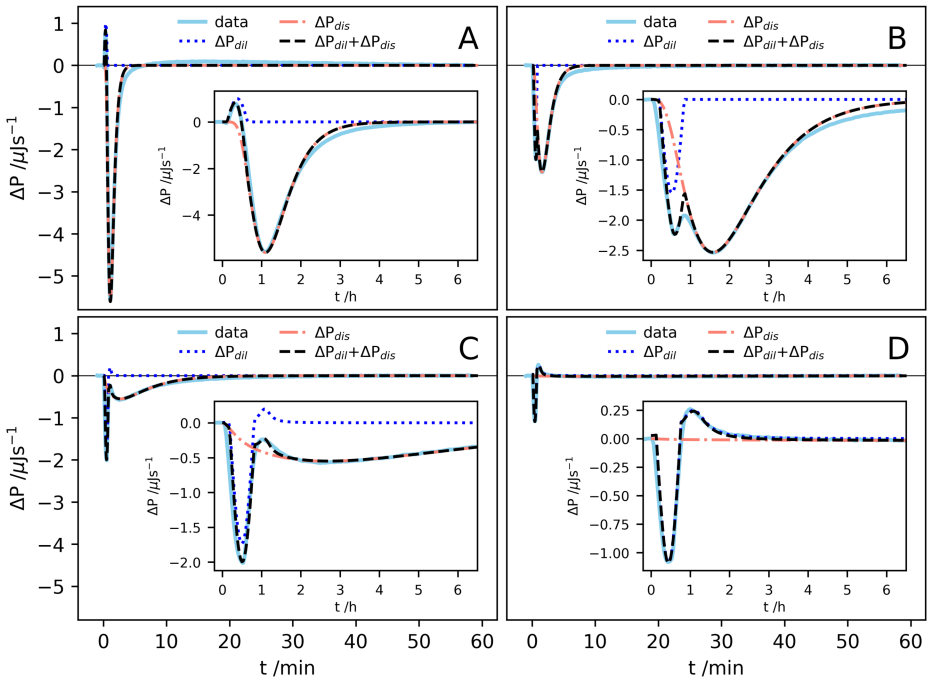

Figure 4.5 Four ΔP traces for ITC injections from both data sets A and B. The injections correspond to a final sample cell concentration of roughly 0.5 mM, 2.1 mM, 4.9 mM and 8.5 mM. The data is shown together with estimates for ΔP_{dis}, ΔP_{dil} and the sum of both.

Estimates of ΔH, for all the processes, are shown in Fig 4.6A, for both data sets A and B. We observe, that ΔH_{dis} seems to have a value of $\Delta H \approx -1.4$ kJmol^{-1} at infinite dilution. We note, that the first points in Fig. 4.6A are associated with some uncertainty due to the large overlap of the two exothermic contributions.

We can further look at the kinetics of the dissolution process by analyzing k^{-1} for the aggregate dissolution as a function c, presented in Fig. 4.6B. We note the strikingly long times needed for dissolution of the peptide aggregates, with the dissolution time at $c = 0$ estimated to 30 s, but eventually increasing to many minutes. For a comparison, we can estimate the diffusion limited dissolution of a spherical particle on the same length scale by using available theory.[98] Such a particle would be fully dissolved after approximately 9 ms.

To explain the observed slow kinetics of the aggregate dissolution, we first note that the dissolution process possibly consists of multiple steps, shown *e.g.* for the A_6K

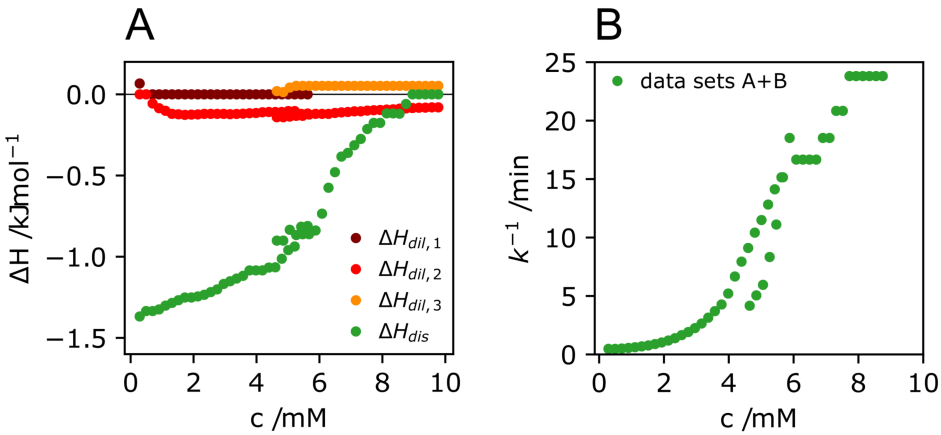

Figure 4.6 (A) ΔH as a function of the total cell concentration after injection for the four processes identified previously. (B) The inverse rate constant for aggregate dissolution, k^{-1}, as a function of concentration.

peptide tubes, which first dissolves into β-sheets before these eventually dissolving to single peptide monomers.[41] Furthermore, we consider the intricate packing structure presented in Chap 3. Every peptide in the structure is assumed to form $n+1$ hydrogen bonds to its neighbor. To remove one peptide from the ribbon structure, multiple hydrogen bonds might need to be broken simultaneously and replaced by water molecules. Each hydrogen bond has a strength of roughly $5-10$ k_BT.[93,99]

4.3 Peptide deprotonation upon assembly

Throughout the work presented in this thesis, we have chosen to not buffer nor alter the pH of the solutions, yet at high concentrations we still observe pH values close to 2. The pH as a function of concentration of A_8K is shown in Fig. 4.7. The peptides are acquired as a trifluoroacetate (TFA) salt and at concentrations below c_s the solution pH is equal to that of the solvent (in this case D_2O), pH $\approx$ 6.24. This means that the peptide-TFA salt can be described as PH^+TFA^-. When the peptides aggregate, the situation is different. The aggregates structure cannot accommodate such a high charge density, as would be the case if every peptide had a net charge of $+1$. Instead the peptides are deprotonated upon assembly, providing an increase in $[H^+]$ as $c-c_s$ and therefore a lowering in the pH.[100] TFA is a strong acid with $pK_a \approx 1$.[101]

The pH data shown in Fig. 4.7 was modeled using a modified version of the equation

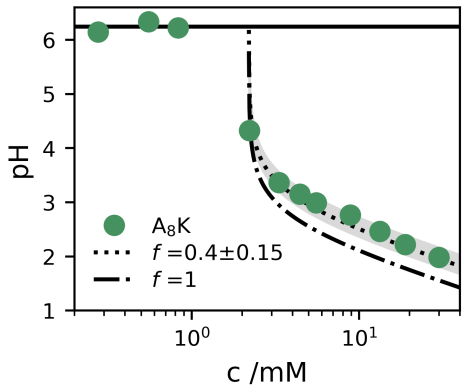

Figure 4.7 pH as a function of A_8K peptide concentration. The solvent pH is shown as a solid line at 6.24. The dotted line represents the calculated pH of a strong acid to represent the deprotonation of the peptide aggregates. This calculation results in $c_s \approx 2$ mM and a charge fraction $f = 0.4 \pm 0.15$. A line corresponding to $f = 1$ is added for clarity.

for a strong acid:

$$pH = -log_{10}\Big((c - c_s)\, f \Big) \tag{4.5}$$

with the addition of a charge fraction, *f*, describing the extent of deprotonated peptides within the aggregates. The data presented in Fig. 4.7 is well described by $f = 0.4$. This tells us, that only roughly half of the peptides in the aggregates are charged. Based on the crystalline structure presented in Chapter 3, we can estimate the surface charge density, $\sigma_0 \approx 96$ mCm^{-2}. c_s as determined from the modeling of the pH measurements only roughly corresponds to the previously determined solubility. This phenomenon of a different protonation state of the molecules in different states is not surprising,[100] but is generally not considered.

4.4 Conclusions

In this chapter, we have had a closer look at the kinetics of the twisted ribbon self-assembly and dissolution in the A_8K and the $A_{10}K$ systems. Using NMR, we could follow the assembly of the crystalline aggregates indirectly by tracking the free monomer concentration as a function of time. We observed kinetics on the timescale of days. This is an effect of the reaction controlled process of peptide aggregate growth. The high hydrogen bond packing results in a high energy barrier for growth, which further leads to a MSZ for peptide growth.

The ΔH for aggregate dissolution of the A_8K aggregates was determined using ITC.

Furthermore, we could see that also the dissolution, like the aggregate growth, had very slow kinetics, which could not be described within the theory for diffusion controlled dissolution.

Finally, we consider the pH of the solution, as this has been observed to change as a function of peptide concentration. We note, that the pH roughly follows the concentration dependence of a strong acid above c_s, indicating that a fraction of the peptides deprotonate upon aggregation. From this fraction of charged peptides in the aggregates, we could determine the surface charge density.

5 Peptide fibrils as rigid rods

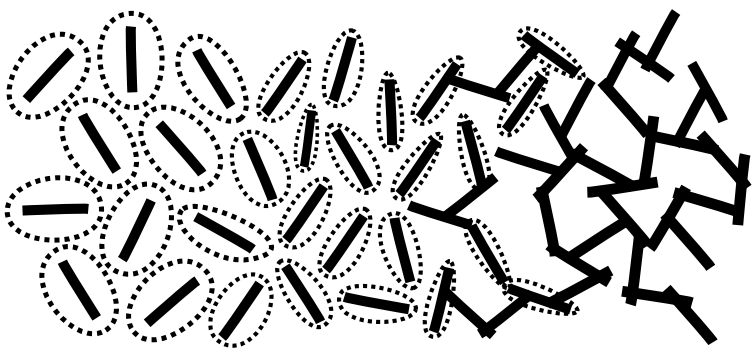

5.1 Dynamical arrest and viscoelastic behavior

Dispersions of elongated objects are interesting from many perspectives.[102] From a fundamental scientific point of view, the presence of shape anisotropy can give rise to interesting phase behavior and viscoelastic behavior otherwise not observed from their spherical counterparts. Many peptide fiber systems form so called peptide hydrogels, where some examples are the DN1, MAX1 and the RADA sequences.[18,26,103] The prefix hydro- is given due to the very high water volume fraction retained in the system. The solid peptide volume fraction can be as low as a couple of percent, sometimes even lower.[26,103] Fundamental understanding of mechanisms behind the gelation in these systems is important from an applications point of view. Furthermore, fibrous systems throughout nature are many, *e.g.* in many viral systems,[104] cellular systems such as actin[105] and in the vast field of amyloid forming peptides and proteins.[6,106] Using simple peptide model systems could help increase the general understanding for these biological phenomena.

The common denominator for systems that transform to a phase that shows a viscoelastic behavior, is the occurrence of dynamical arrest.[102] There are many factors that can contribute to this arrest, but to describe the underlying mechanism, we will first consider a dispersion of stiff monodisperse rods at various concentrations and of a rather high aspect ratio, L/d, where L is the rod length and d is the diameter. If the concentration is dilute, the rods rarely interact with each other and the viscous properties of the dispersion is the same as that of the solvent. In this dilute concentration regime, often defined by the limit $\phi < 1/L^3$,[107] the rods can diffuse freely. This typically occurs by rotation, with a corresponding diffusion coefficient, D_r, or by translation, D_t, which in turn can be either perpendicular, $D_\perp$, or parallel, $D_\parallel$, to the rod axis. Due to the rotational motion, one usually considers the excluded volume of the rod to take up roughly a sphere with the diameter L as is illustrated in Fig. 5.1A.

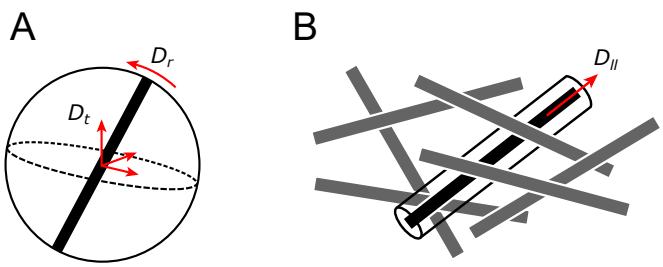

Figure 5.1 (A) dilute rod dispersion and (B) a concentrated dispersion.

On increasing the concentration, one eventually reaches a concentration where the whole sample space is occupied by the excluded volume spheres of the diffusing rods,

Fig. 5.1A. This concentration is referred to as the overlap concentration and is essentially determined by the rod geometry $\phi^* = (d/L)^2$. Above this concentration, the likelihood for rods to interact is high. Both D_r and $D_\perp$ become increasingly limited, as the accessible volume for the rods is limited to a cylinder of a slightly larger d, Fig 5.1B, whereas $D_\parallel$ is not affected.

The dynamics in the $A_{10}K$ systems has been traced using DLS, Fig. 5.2. Due to the rather short length of the ribbons, we are not able to measure the rotational diffusion, as this requires $qL > 1$. We therefore interpret the correlation function $C(t)$ as a result of purely translational diffusion. For the lowest concentration, we observe essentially a single exponential decay, which can be described as an average of the parallel and the perpendicular modes, $D_\parallel$ and $D_\perp$, Fig 5.2. This average is given by[108]

$$D_t = \frac{1}{3}D_\parallel + \frac{2}{3}D_\perp \tag{5.1}$$

The lowest concentration data was analyzed using a second order cumulant analysis. This resulted in $D_t \approx 7\times10^{-12}$ m^{2}s^{-1} and a Z-average aggregate length of $\langle L\rangle = 300$ nm with a polydispersity index of 0.31.

Increasing the peptide volume fraction, we see that the correlation functions no longer show a monomodal decay, Fig. 5.2. As an insert in Fig. 5.2, we also show how $g^{(2)}(0) - 1$ decreases. Both these features indicate the presence of a dynamical arrest. The dynamical arrest of spherical colloids has been studied extensively,[109,110] and the high concentration correlation functions from our system resemble the decay of a system close to the glass transition. However, not only does the glass transition volume fraction, ϕ_g, for spheres occur much higher, $\phi_g = 0.58$, but the arrest of the translational diffusion is isotropic. For rods this is not the case, as discussed in the context of Fig. 5.1.

The interpretation of the bimodal decay presented for the higher concentrations in Fig. 5.2 is not trivial. In previous studies, these have been assumed to correspond to $D_\parallel$ and $D_\perp$,[39,111] but the slow mode could also be an effect of self-diffusion,[112,113] or the β-relaxation mode in a glassy system.[109,110]

This observed dynamical arrest has strong effects of the relaxation of applied stresses to the system. The time it takes for a system to relax an applied stress is called the stress relaxation time, τ, and occurs mainly due to rotational diffusion, $\tau \sim 1/D_r$.[114] As the rotational diffusion is strongly limited above ϕ^*, τ becomes increasingly long. A system where the relaxation time is long will also present corresponding macroscopical properties, *i.e.* behave more solid-like. A way of determining τ is from an oscillatory strain measurement in a rheometer where the complex modulus $G^* = G' + iG''$ is measured as a function of oscillation frequency. In Fig. 5.3A we show the storage and

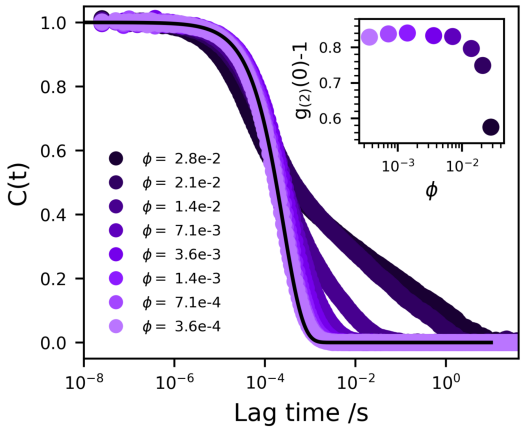

Figure 5.2 Normalized auto-correlation function $C(t)$ as a function of ϕ for $A_{10}K$. At low concentrations $C(t)$ can be assumed to follow a monomodal exponential decay. As the concentration increases, this breaks down due to dynamical arrest. The insert shows $g_{(2)}(0) - 1$.

loss moduli G' and G'' respectively for varying frequencies of deformation. When τ is long, the system does not have the time to relax before the next oscillation and $G' > G''$ and vice versa. The relaxation time is extracted in the point where $G' = G''$. In the $A_{10}K$ system this cross-over is not visible and furthermore, the moduli are more or less independent of frequency. We therefore got $\tau \gg 1/\omega_{\min} = 100$ s, for a concentration of only $\phi \approx 0.039$.

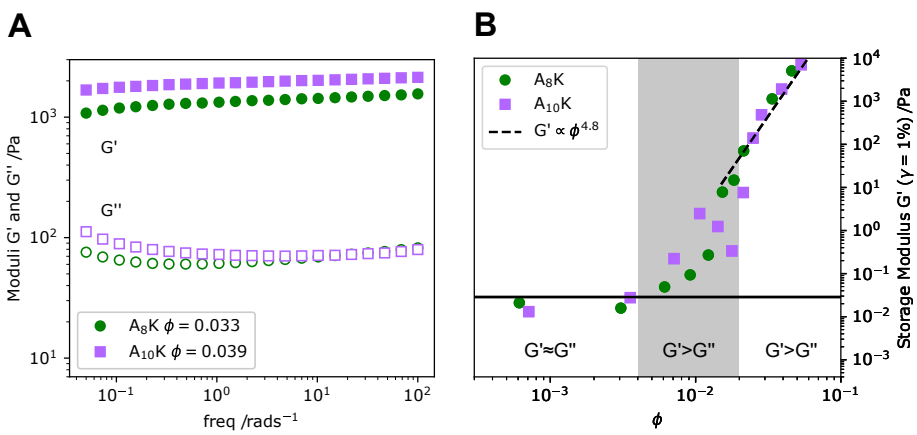

Figure 5.3 (A) Frequency sweeps for A_8K and $A_{10}K$ respectively at $\gamma = 1$ % showing that the moduli are more or less frequency independent and therefore has a very long τ. (B) G' at $\omega = 1$ rads^{-1} and $\gamma = 1$ % as a function of sample concentration for A_8K and $A_{10}K$ respectively. Above $\phi \approx 0.005$ the systems show $G' > G''$. The increase in G' with ϕ can be roughly described by a power-law behavior $G' \propto \phi^n$, where $n = 5$ is shown in the figure.

We further analyze the system with oscillatory rheology in the linear viscoelastic regime by obtaining the frequency at 1 % amplitude as a function of concentration, Fig. 5.3B. A first viscoelastic response is observed above a concentration of $\phi \approx 0.005$, similar to the concentration where the correlation function in Fig. 5.2 starts to deviate from a monoexponential decay. This is in agreement with the estimate of the overlap concentration, $\phi^* \approx 0.0036$. Above $\phi \approx 0.02$, we observe that G' increases approximately as a power-law $G' \propto \phi^n$, where a fit to the data results in $n = 4.8$. This is high when comparing to other systems of peptide fibers[26,115] or other biological fibers in general.[116,117] These systems are better described using models for the scaling behavior of semi-flexible and rigid polymers which predict $n \approx 2 - 2.5$ depending on the fiber properties.[105,118]

A strong concentration dependence of the storage modulus has been found at certain pH and ionic strength values in the fiber forming peptide system FEFEFKFK[119] and in nanocrystalline cellulose (NCC).[120] In both cases, the anisotropic particles have a very high rigidity. A model to describe the storage modulus behavior, including the effects of attractive or repulsive particle interactions, was devised by Hill.[121] The model equation of the G' as a function of ϕ is given by

$$G' \sim \beta E \phi^{11/3} (1 + \alpha\phi)^{10/3} \tag{5.2}$$

where E is the Young's modulus, β is an order one constant and α is a constant describing the interactions in the system. If the system is attractive, $\alpha > 0$ and vice versa. For the model to be valid the rods should have more than 2.5 contacts per rod.

The rather high rigidity of amyloid-like fibers is proposed to be directly correlated to the hydrogen bond density inside the fiber.[122] Using an equation presented by Knowles et al.,[122] we estimate the Young's modulus of the A_nK fibers to $E \approx 32$ GPa, comparable to the modulus of spider silk.[3] This is higher than other amyloid-like fibrils, suggesting that these fibers indeed are stiffer than others ($0.3 - 4$ GPa),[123] and further suggesting that the hydrogen bonding density is higher in the A_nK fibers than in amyloids in general. The main reason for this is probably the large quantity of A in the peptides, one of the smallest amino acids. Most amyloid forming systems have a higher variation in the peptide sequence, resulting in large side groups that can interfere with an optimal hydrogen bonding density.

5.2 Rod interactions

We previously showed how we reach arrested dynamics only by considering an increase in concentration and how the fibers from the A_8K and $A_{10}K$ peptides are stiffer than

other peptide fibers. However, the transition from a liquid to a system with an elastic response in rod systems also depends on further rod properties, such as their interparticle interactions.[102] The A_8K and $A_{10}K$ fibers have been shown to be colloidally stable due to electrostatic repulsion.[39,75] We further note that peptides generally are amphiphilic molecules and that peptide and protein aggregates generally present hydrophobic patches on their surface.[124,125] In Chapter 3, we saw that the fibers formed from the A_8K and the $A_{10}K$ have a limited number of laminated β-sheets giving rise to accessible hydrophobic surface. The combination of both electrostatic repulsion and hydrophobic attraction can further spice up the phase behavior, and such a system is reminiscent of those that have a DLVO potential.[4,125,126]

The repulsiveness of charged systems in solution is based on the formation of an electrostatic double layer, where counter-ions in solution will gather in the vicinity of the charged surface.[4] When two charged entities approach each other their electrostatic clouds will overlap before their hard excluded volumes do. This leads to an increase in the osmotic pressure and thus, repulsion. One can consider the charged particles to have an effectively larger volume fraction ϕ_{eff}.

To characterize the interactions of the studied peptide system, dispersions of $A_{10}K$ aggregates were analyzed as a function of added NaCl. By the addition of salt, we changed the ionic strength of the system and consequently the Debye screening length, κ^{-1}. At zero salt concentration, the gel-like dispersions were found to be transparent, indicating a homogeneous mixture. An example is shown in Fig. 5.4. However, when 0.1 M NaCl was added, the dispersions instead became opaque. The light passing through is scattered on what is likely heterogeneous clusters. These clusters have formed because increased ionic strength screens the electrostatic repulsion to such an extent that the hydrophobic attraction becomes predominant.

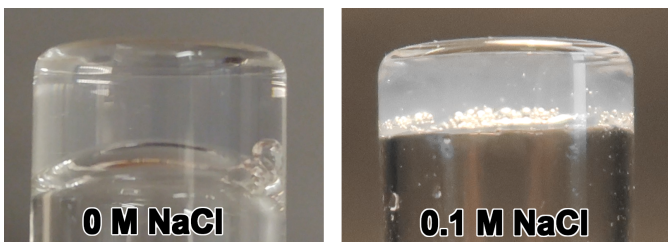

Figure 5.4 Images of an $A_{10}K$ peptide hydrogel at $\phi \approx 0.025$ in pure water (left) and in 0.1 M NaCl (right).

The dispersions were further analyzed using SAXS measurements, from which we could conclude that the integrity of the individual fibers were not affected, see Paper VII. However, an increased slope was observed in the low q-regime, Fig. 5.5A. The scattering pattern can be described by $I(q) = C\langle P(q)\rangle S_{\text{eff}}(q)$, where C is a

constant, $\langle P(q) \rangle$ is the orientationally averaged form factor and $S_{\text{eff}}(q)$ the effective structure factor. With a constant $\langle P(q) \rangle$ of the fibers, the change in the scattering curve must be due to a change in $S_{\text{eff}}(q)$. A slope of $I(q) \propto q^{-1.5}$ could indicate the formation of fiber clusters.[102]

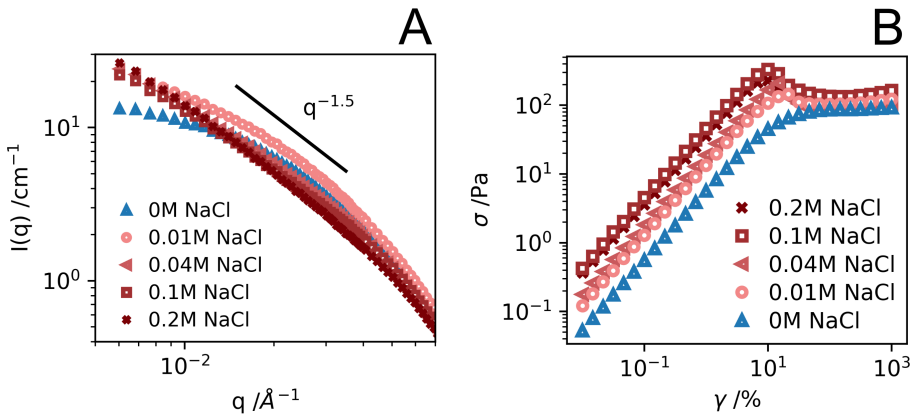

Figure 5.5 (A) SAXS patterns of $\phi = 0.025$ $A_{10}K$ dispersions at varying concentration of NaCl. An increase is observed at lower q-values, indicating an increase in $S_{\text{eff}}(q)$. A final slope of $I(q) \propto -1.5$ is found for [NaCl]=0.2 M. (B) An oscillatory amplitude sweep with $\sigma(\gamma)$. At low γ the deformation is elastic but above a certain transition value $\gamma \approx 10$ % the deformation becomes plastic. With the introduction of NaCl in the sample an increasing amount of stress is needed to reach the plastic deformation.

The non-linear rheological response of the system is also affected by the salt addition. In an oscillatory measurement, where we trace the stress amplitude, σ, as a function of strain, γ, we can see how the gels at first show a purely elastic behavior before transitioning to a regime where σ is independent of γ, Fig. 5.5B. In this final regime, the deformation is plastic, meaning that the network is destroyed and the rods are displaced with regards to each other. A stress overshoot at ($\gamma \approx 10$ %) shows, that when the electrostatics are screened, a higher stress is needed to disrupt the network. Indeed, the stress needed to overcome the attractive hydrophobic force of the rods is expected to be higher.[54]

The experiments are in full agreement with one another. At zero salt, the system is dominated by repulsive interactions meaning that the system is characterized as a soft repulsive glass.[44] We note, that the lower glass transition concentration for rods has been determined to $\phi_g \approx 0.7d/L$.[127] With $L/d \approx 10$, $A_{10}K$ has a hard rod volume fraction $\phi < \phi_g$. However, due to the effectively larger volume fraction from electrostatic repulsion ϕ_{eff}, we do indeed reach above ϕ_g. As we introduce salt in the system, we reduce ϕ_{eff} and the probability for the rods to interact through hydrophobic attraction increases until reaching a predominantly attractive regime.

An illustration of the different arrested in the two regimes is shown in Fig. 5.6.

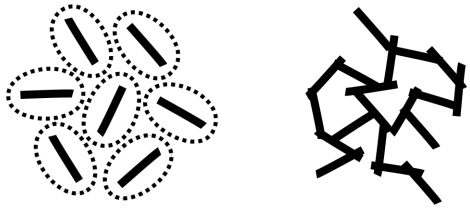

Figure 5.6 A schematic of charged rods at zero salt (left) where the electrostatic double layer leads to an effective diameter larger than the hard rod diameter. When salt is added the electrostatics are screened the attractive interactions lead to rod aggregation and gel formation.

5.3 Liquid crystal transition

As stated previously, anisotropic particles in shape have the ability to show a richer phase behavior than regular spherical particles.[102] These phases arise from the possibility of orientational ordering as well as various levels of positional ordering. Due to this lack of complete isotropy, as in liquids, but also not complete ordering as in solid crystals, these phases are often referred to as liquid crystalline phases.[128]

In the simplest case, the nematic phase, there is only orientational ordering. The existence of nematic phases in nature has been known for more than a century, but the theoretical explanation of the formation of nematic phases from rod dispersions was not formalized until the middle of the 20$^{\text{th}}$ century by Onsager.[129] Onsager stated that the driving force for the formation of the nematic phase was purely entropic. Although the orientational ordering results in a decrease in entropy, a second entropic contribution, the translational entropy, strongly favors rod alignment. The concentration, at which the transition from isotropic to nematic in a solution of long and thin rods occurs, was determined to $\phi_{\text{IN}} \approx 4/r$.

A_8K and $A_{10}K$ peptides behave as stiff rods in solution and are therefore expected to have a transition from an isotropic to a liquid crystalline phase. This transition was studied by studying the samples between crossed polarization filters. A photo series of varying concentrations of $A_{10}K$ is shown in Fig. 5.7. For concentrations where $\phi > 0.02$, we observed birefringence (bright light) throughout the samples, whereas for $\phi < 0.02$, the samples were completely dark. Birefringence is an effect arising from the interaction between polarized light and the sample. If the sample consists of oriented entities, it can alter the polarization of the light and thereby transmit it through a second polarization filter, placed at a 90° angle to the first one. The formed phase is presumably nematic, as the large polydispersity hinders further ordering of the

aggregates.[130] The phase transition for $A_{10}K$ is determined to $\phi_{IN} \approx 0.02$, whereas the same transition A_8K occurs at a higher volume fraction $\phi_{IN} \approx 0.1$

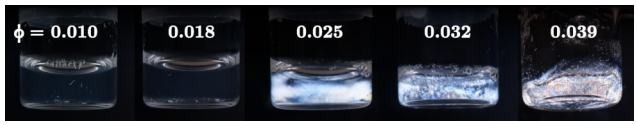

Figure 5.7 Photographs of an $A_{10}K$ solution between perpendicular oriented polarization filters. Above $\phi \approx 0.02$ the samples show birefringence indicating the presence of a liquid crystal ordering of the rods in solution.

The difference in ϕ_{IN} is somewhat surprising, as the longer A_8K would be expected to have a lower ϕ_{IN}. However, the ribbon aggregates have previously been shown to be repulsive, exhibiting an effectively larger volume fraction. The effect on ϕ_{IN} in charged systems was introduced by Stroobants et al.,[131]. Apart from the effective volume fraction, a *twisting* term is introduced. This accounts for the fact that charged rods have their lowest energy configuration when they are perpendicular to each other, as opposed to being parallel.

To explain the observed discrepancy in ϕ_{IN} for the two peptides, we need to consider that the non-aggregated peptide monomers are charged species and will therefore contribute to the ionic strength of the solution. As the peptide solubility of $A_{10}K$ is very low, $\phi_s \approx 5 \times 10^{-6}$ (≈ 7 μM), the electrostatic screening can basically be neglected. For A_8K on the other hand, $\phi_s \approx 0.001$ (≈ 2 mM). If we assume that the monomers can be considered a simple 1:1 electrolyte, we get a corresponding Debye length, $\kappa^{-1} \approx 7$ nm, *i.e.* a significant screening of the A_8K aggregates. We note that by using Onsager's prediction on the A_8K rods, with $L = 180$ and $d = 6$, we estimated $\phi_{IN} \approx 0.13$, not too far away from the observed $\phi_{IN} \approx 0.1$. We are therefore rather close to the hard rod case.

Due to the deprotonation of the peptides when they undergo assembly, introduced in Chapter 4, the screening from the $[H^+]$ concentration will depend on the total peptide concentration. Together with the high polydispersity, the result is most likely a very broad two-phase region between the isotropic and the nematic phases. Finally, we note the similarity between the A_8K and $A_{10}K$ systems from both linear and non-linear rheology. This suggests that only a small fraction of the sample has transitioned to a nematic.

5.4 Flow behavior

A common feature of rods in solution is that they align upon an applied shear.[132] This leads to a shear thinning behavior where the viscosity decreases as the shear rate is increased, observed experimentally for both peptide systems, Fig. 5.8. We note, that the samples show a maximum shear-thinning, $\eta \propto \dot{\gamma}^{-1}$ within the whole experimental shear rate range. Furthermore, the shear thinning behavior in the $A_{10}K$ hydrogel is shown to be fully reversible.

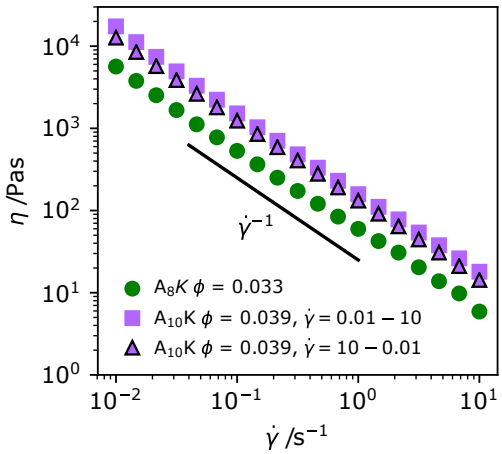

Figure 5.8 A flow curve experiment for A_8K and $A_{10}K$ respectively, where both systems show maximum shear thinning $\eta \propto \dot{\gamma}^{-1}$.

Alignment is not an implicit effect in shear-thinning peptide fiber system. In the MAX1 system it was found, that the shear thinning occurs through rupture of the peptide fiber network.[133] The fibers were simply too long to align. Although we cannot exclude network rupture during shear of the A_8K and the $A_{10}K$ systems, alignment has been shown to occur.[76]

5.5 Conclusions

In this chapter we have looked at how the peptide aggregates from A_8K and $A_{10}K$ behave in solution and how dynamical arrest can occur as the concentration is increased. By arrest of D_r and $D_\perp$, the stress relaxation time τ becomes close to infinite for rather low peptide concentrations. This indicates that the fibers formed in these systems are very rigid. This notion is reinforced in the interpretation of the very high concentration dependence of the storage modulus G'. From a model used to describe similarly

strong concentration dependence of G' in NCC, we estimate a Young's modulus of the $A_{10}K$ fibers to roughly 30 GPa. This high rigidity is mainly an effect of the higher hydrogen bond density in comparison to other amyloid forming peptides.[122]

We have also learned, that although the peptides are colloidaly stable in aqueous solution, the rods are still hydrophobically attractive. Upon the screening of the electrostatic repulsion, we observe how the interactions are inverted and that the peptides aggregate to larger clusters. This behavior is similar to what one would expect in systems with a DLVO-like potential.[4,125,126] Based on the observed interactions, the gel-like sample formed by the fibers in pure water should be classified as a repulsive glass that with the increased ionic strength turns into an attractive gel.[44]

Due to the anisotropic shape of the fibers, the system undergoes a phase transition from an isotropic to an ordered liquid crystalline phase, presumably nematic. Again the interactions in the system play a role as the electrostatic double layer acts as an effectively larger rod diameter. The transition can therefore occur at a much lower concentration than expected for hard rods. We have also seen that this phase can be induced by subjecting the system to a shear.

6 Epilogue

To wrap up this thesis, I will place some final comments on the context of the thesis and of the findings. Specifically, I will look at the comparison between the A_nK system and general amyloid forming systems. What are the main similarities and what are the main differences? I will also present some possible prospects of the A_nK self-assembly studies.

Many studies of the self-assembly of shorter peptide sequences has originated from the field of amyloids, by simply selecting the amino acids that take part in the β-sheet formation [134]. This results in a high (natural) amino acid variability of the sequence. The A_nK peptides, on the other hand, are from the same perspective rather simple, only containing two different amino acids. This is also what facilitates the systematic studies of for example varying the peptide length. The comparison between the A_nK peptides and peptides that form amyloids is therefore not always trivial.

From a general structural point of view, we can conclude that the A_nK ribbons and amyloids indeed are somewhat similar. The structures are fibrillar and contain β-sheets, extending in the propagation direction of the ribbon-like structures. Growth occurs through the extension of these β-sheets, which results in the observed slow growth kinetics. However, an important difference is the internal ordering of the peptides within the aggregates. In A_nK, the β-sheets laminated to form a dense crystalline structure. Amyloid fibers, on the other hand, typically contain both crystalline and amorphous regions. This has, as we have seen, a large impact on the colloidal properties of the fibers [135].

When comparing self-assembled peptide fibers, another important aspect is that of colloidal stability. The difference in colloidal stability will govern if a more concentrated dispersion of fibers form a glass, a hydrogel or precipitates of fiber bundles. Here the direct comparison between the studied system and other amyloids is not as conclusive. We have simply not aimed at performing measurements in physiological-like conditions. However, a very important property of all peptides is that of being

both electrostatically repulsive and hydrophobically attractive[125,126]. Exactly how it shows boils down to peptide sequence, structure deformation (twist etc.), solution ionic strength, and much more.

Often when you answer a question in science, new ones appear. To continue the work on understanding the self-assembly of the A_nK model peptide specifically or model peptide systems in general, I have identified some questions that I find particularly interesting.

The first is to further investigate the chirality of the self-assembled aggregates, as the underlying thermodynamic reasons for this are still under debate. This can be done by exchanging amino acids in the peptide sequence with glycine: the only non chiral amino acid. One could also consider mixing both L and D-amino acids. Further studies of how the twist of the fibers is affected by the solvent and its properties are also important[82].

The thermodynamic models for the assembled structures can be fine-tuned to serve as a better description of reality. It would be important to try to minimize the amount of input parameters to make the model even more robust. For this a great deal of work is needed, both experimental and theoretical, specifically on the chirality.

Further topics where one could continue the studies is the phase behavior of the A_8K and the $A_{10}K$ peptide ribbons. Is it possible to, in more detail, map up the phase diagram of the ribbon forming A_8K and $A_{10}K$ peptides including the limits of the observed nematic, is it possible to determine an order parameter? In order to do this it might also be worthwhile to further look into the complexity of the electrostatic screening due to both individual peptide monomers and background $[H^+]$.

I would finally like to emphasize the fact that the A_nK peptides are model peptides, and that we have not considered the applicability of the system in this thesis work. The production of very hydrophobic peptides, such as the longer $A_{10}K$ peptide, is typically associated with both problematic yield and purity.

References

[1] Whitesides, G. M.; Grzybowski, B. Self-Assembly at All Scales. *Science* **2002**, *295*, 2418–2421.

[2] Makam, P.; Gazit, E. Minimalistic Peptide Supramolecular Co-Assembly: Expanding the Conformational Space for Nanotechnology. *Chemical Society Reviews* **2018**, *47*, 3406–3420.

[3] Porter, D.; Guan, J.; Vollrath, F. Spider Silk: Super Material or Thin Fibre? *Advanced Materials* **2013**, *25*, 1275–1279.

[4] Evans, D. F.; Wennerström, H. *The Colloidal Domain: Where Physics, Chemistry, Biology and Technology Meet*, 2nd ed.; Wiley-VCH: New York, 1999.

[5] Mendes, A. C.; Baran, E. T.; Reis, R. L.; Azevedo, H. S. Self-Assembly in Nature: Using the Principles of Nature to Create Complex Nanobiomaterials. *WIREs Nanomedicine and Nanobiotechnology* **2013**, *5*, 582–612.

[6] Dobson, C. M. Protein Misfolding, Evolution and Disease. *Trends in Biochemical Sciences* **1999**, *24*, 329–332.

[7] Semino, C. E. Self-Assembling Peptides: From Bio-Inspired Materials to Bone Regeneration. *Journal of Dental Research* **2008**, *87*, 606–616.

[8] Fosgerau, K.; Hoffmann, T. Peptide Therapeutics: Current Status and Future Directions. *Drug Discovery Today* **2015**, *20*, 122–128.

[9] Schulz, G. E.; Schirmer, R. H. *Principles of Protein Structure*; Springer Advanced Texts in Chemistry 1; Springer-Verlag, 1985.

[10] Abel, E. W., Ed. *Tutorial Chemistry Texts*; Royal Society of Chemistry: Cambridge, 2007; pp 1–19.

[11] Zhao, X.; Pan, F.; Xu, H.; Yaseen, M.; Shan, H.; E. Hauser, C. A.; Zhang, S.; R. Lu, J. Molecular Self-Assembly and Applications of Designer Peptide Amphiphiles. *Chemical Society Reviews* **2010**, *39*, 3480–3498.

[12] Dill, K. A. Dominant Forces in Protein Folding. *Biochemistry* **1990**, *29*, 7133–7155.

[13] Harano, Y.; Kinoshita, M. Large Gain in Translational Entropy of Water Is a Major Driving Force in Protein Folding. *Chemical Physics Letters* **2004**, *399*, 342–348.

[14] Colombo, G.; Soto, P.; Gazit, E. Peptide Self-Assembly at the Nanoscale: A Challenging Target for Computational and Experimental Biotechnology. *Trends in Biotechnology* **2007**, *25*, 211–218.

[15] Zhang, S. Fabrication of Novel Biomaterials through Molecular Self-Assembly. *Nature Biotechnology* **2003**, *21*, 1171–1178.

[16] Zhang, S.; Holmes, T.; Lockshin, C.; Rich, A. Spontaneous Assembly of a Self-Complementary Oligopeptide to Form a Stable Macroscopic Membrane. *Proceedings of the National Academy of Sciences of the United States of America* **1993**, *90*, 3334–3338.

[17] Hauser, C. A. E.; Zhang, S. Designer Self-Assembling Peptide Nanofiber Biological Materials. *Chemical Society Reviews* **2010**, *39*, 2780–2790.

[18] Aggeli, A.; Bell, M.; Boden, N.; Keen, J. N.; Knowles, P. F.; McLeish, T. C. B.; Pitkeathly, M.; Radford, S. E. Responsive Gels Formed by the Spontaneous Self-Assembly of Peptides into Polymeric β-Sheet Tapes. *Nature* **1997**, *386*, 259–262.

[19] Aggeli, A.; Bell, M.; Boden, N.; Keen, J. N.; McLeish, T. C. B.; Nyrkova, I.; Radford, S. E.; Semenov, A. Engineering of Peptide β-Sheetnanotapes. *Journal of Materials Chemistry* **1997**, *7*, 1135–1145.

[20] Blake, C.; Serpell, L. Synchrotron X-Ray Studies Suggest That the Core of the Transthyretin Amyloid Fibril Is a Continuous β-Sheet Helix. *Structure* **1996**, *4*, 989–998.

[21] Balbach, J. J.; Ishii, Y.; Antzutkin, O. N.; Leapman, R. D.; Rizzo, N. W.; Dyda, F.; Reed, J.; Tycko, R. Amyloid Fibril Formation by Aβ16-22, a Seven-Residue Fragment of the Alzheimer's β-Amyloid Peptide, and Structural Characterization by Solid State NMR. *Biochemistry* **2000**, *39*, 13748–13759.

[22] Gilead, S.; Gazit, E. Self-Organization of Short Peptide Fragments: From Amyloid Fibrils to Nanoscale Supramolecular Assemblies. *Supramolecular Chemistry* **2005**, *17*, 87–92.

[23] Ulijn, R. V.; Smith, A. M. Designing Peptide Based Nanomaterials. *Chemical Society Reviews* **2008**, *37*, 664–675.

[24] Zhao, Y.; Yang, W.; Chen, C.; Wang, J.; Zhang, L.; Xu, H. Rational Design and Self-Assembly of Short Amphiphilic Peptides and Applications. *Current Opinion in Colloid & Interface Science* **2018**, *35*, 112–123.

[25] Holmes, T. C.; de Lacalle, S.; Su, X.; Liu, G.; Rich, A.; Zhang, S. Extensive Neurite Outgrowth and Active Synapse Formation on Self-Assembling Peptide Scaffolds. *Proceedings of the National Academy of Sciences* **2000**, *97*, 6728–6733.

[26] Schneider, J. P.; Pochan, D. J.; Ozbas, B.; Rajagopal, K.; Pakstis, L.; Kretsinger, J. Responsive Hydrogels from the Intramolecular Folding and Self-Assembly of a Designed Peptide. *Journal of the American Chemical Society* **2002**, *124*, 15030–15037.

[27] Pochan, D. J.; Schneider, J. P.; Kretsinger, J.; Ozbas, B.; Rajagopal, K.; Haines, L. Thermally Reversible Hydrogels via Intramolecular Folding and Consequent Self-Assembly of a de Novo Designed Peptide. *Journal of the American Chemical Society* **2003**, *125*, 11802–11803.

[28] Pandya, M. J.; Spooner, G. M.; Sunde, M.; Thorpe, J. R.; Rodger, A.; Woolfson, D. N. Sticky-End Assembly of a Designed Peptide Fiber Provides Insight into Protein Fibrillogenesis. *Biochemistry* **2000**, *39*, 8728–8734.

[29] Hill, R. B.; Raleigh, D. P.; Lombardi, A.; DeGrado, W. F. De Novo Design of Helical Bundles as Models for Understanding Protein Folding and Function. *Accounts of Chemical Research* **2000**, *33*, 745–754.

[30] Tian, Y.; Polzer, F. B.; Zhang, H. V.; Kiick, K. L.; Saven, J. G.; Pochan, D. J. Nanotubes, Plates, and Needles: Pathway-Dependent Self-Assembly of Computationally Designed Peptides. *Biomacromolecules* **2018**, *19*, 4286–4298.

[31] Gazit, E. A Possible Role for π-Stacking in the Self-Assembly of Amyloid Fibrils. *The FASEB Journal* **2002**, *16*, 77–83.

[32] Reches, M.; Gazit, E. Casting Metal Nanowires Within Discrete Self-Assembled Peptide Nanotubes. *Science* **2003**, *300*, 625–627.

[33] Gazit, E. Self-Assembled Peptide Nanostructures: The Design of Molecular Building Blocks and Their Technological Utilization. *Chemical Society Reviews* **2007**, *36*, 1263–1269.

[34] Luo, Z.; Zhang, S. Designer Nanomaterials Using Chiral Self-Assembling Peptide Systems and Their Emerging Benefit for Society. *Chemical Society Reviews* **2012**, *41*, 4736–4754.

[35] Mandal, D.; Shirazi, A. N.; Parang, K. Self-Assembly of Peptides to Nanostructures. *Organic & biomolecular chemistry* **2014**, *12*, 3544–3561.

[36] Bera, S.; Gazit, E. Self-Assembly of Functional Nanostructures by Short Helical Peptide Building Blocks. *Protein and Peptide Letters* **2019**, *26*, 88–97.

[37] Vauthey, S.; Santoso, S.; Gong, H.; Watson, N.; Zhang, S. Molecular Self-Assembly of Surfactant-like Peptides to Form Nanotubes and Nanovesicles. *Proceedings of the National Academy of Sciences* **2002**, *99*, 5355–5360.

[38] von Maltzahn, G.; Vauthey, S.; Santoso, S.; Zhang, S. Positively Charged Surfactant-like Peptides Self-Assemble into Nanostructures. *Langmuir* **2003**, *19*, 4332–4337.

[39] Cenker, Ç. Ç.; Bucak, S.; Olsson, U. Aqueous Self-Assembly within the Homologous Peptide Series AnK. *Langmuir* **2014**, *30*, 10072–10079.

[40] Cenker, Ç. Ç.; Bucak, S.; Olsson, U. Nanotubes and Bilayers in a Model Peptide System. *Soft Matter* **2011**, *7*, 4868–4875.

[41] Cenker, Ç. Ç.; Bomans, P. H. H.; Friedrich, H.; Dedeoğlu, B.; Aviyente, V.; Olsson, U.; Sommerdijk, N. A. J. M.; Bucak, S. Peptide Nanotube Formation: A Crystal Growth Process. *Soft Matter* **2012**, *8*, 7463–7470.

[42] Nyrkova, I. A.; Semenov, A. N.; Aggeli, A.; Boden, N. Fibril Stability in Solutions of Twisted -Sheet Peptides: A New Kind of Micellization in Chiral Systems. *The European Physical Journal B - Condensed Matter and Complex Systems* **2000**, *17*, 481–497.

[43] Aggeli, A.; Nyrkova, I. A.; Bell, M.; Harding, R.; Carrick, L.; McLeish, T. C. B.; Semenov, A. N.; Boden, N. Hierarchical Self-Assembly of Chiral Rod-like Molecules as a Model for Peptide β-Sheet Tapes, Ribbons, Fibrils, and Fibers. *Proceedings of the National Academy of Sciences* **2001**, *98*, 11857–11862.

[44] Zaccarelli, E. Colloidal Gels: Equilibrium and Non-Equilibrium Routes. *Journal of Physics: Condensed Matter* **2007**, *19*, 323101.

[45] Lindner, P., Zhemb, T., Eds. *Neutrons, X-Rays and Light: Scattering Methods Applied to Soft Condensed Matter*; Noth-Holland Delta Series; Elsevier Science B.V.: Amsterdam, 2002.

[46] de Jeu, W. H. *Basic X-Ray Scattering for Soft Matter*; Oxford University Press, 2016.

[47] Zorn, R. In *Physics of Life: Lecture Notes of the 49th IFF Spring School 2018*; Gompper, G., Dhont, J. K. G., Elgeti, J., Falke, C., Fedosov, D., Förster, S., Lettinga, P., Offenhäuser, A., Eds.; Schriften Des Forschunszentrum Jülich Reihe Schlüsseltechnologien/Key Technologies; Forschungszentrum Jülich GmbH Zentralbibliothek, Verlag: Jülich, 2018; Vol. 158.

[48] Pedersen, J. S. In *Neutrons, X-Rays and Light Scattering Methods Applied to Soft Condensed Matter*; Lindner, P., Zemb, T., Eds.; North-Holland Delta Series; Elsevier Science B.V.: Amsterdam, 2002.

[49] Doucet, M. Et al. SasView Version 4.1.2, Zenodo, 10.5281/Zenodo.825675.

[50] Pusey, P. N. In *Neutron, X-Rays and Light: Scattering Methods Applied to Soft Condensed Matter*; Lindner, P., Zemb, T., Eds.; North-Holland Delta Series; Elsevier Science B.V.: Amsterdam, 2002.

[51] Schätzel, K. Correlation Techniques in Dynamic Light Scattering. *Applied Physics B* **1987**, *42*, 193–213.

[52] Koppel, D. E. Analysis of Macromolecular Polydispersity in Intensity Correlation Spectroscopy: The Method of Cumulants. *The Journal of Chemical Physics* **1972**, *57*, 4814–4820.

[53] Pusey, P. N. In *Neutrons, X-Rays and Light Scattering Methods Applied to Soft Condensed Matter*; Lindner, P., Zemb, T., Eds.; North-Holland Delta Series; Elsevier Science B.V.: Amsterdam, 2002.

[54] Mewis, J.; Wagner, N. J. *Colloidal Suspension Rheology*; Cambridge Series in Chemical Engineering; Cambridge University Press: Cambridge, 2012.

[55] Larson, R. G. *The Structure and Rheology of Complex Fluids*; Topics in Chemical Engineering; Oxford University Press: NewYork, 1999.

[56] Sathaye, S.; Mbi, A.; Sonmez, C.; Chen, Y.; Blair, D. L.; Schneider, J. P.; Pochan, D. J. Rheology of Peptide- and Protein-Based Physical Hydrogels: Are Everyday Measurements Just Scratching the Surface? *Wiley Interdisciplinary Reviews: Nanomedicine and Nanobiotechnology* **2015**, *7*, 34–68.

[57] Yan, C.; Pochan, D. J. Rheological Properties of Peptide-Based Hydrogels for Biomedical and Other Applications. *Chemical Society Reviews* **2010**, *39*, 3528–3540.

[58] Bovey, F. A.; Mirau, P. A. *NMR of Polymers*; Academic Press: San Diego, 1996; pp 1–115.

[59] Bharti, S. K.; Roy, R. Quantitative 1H NMR Spectroscopy. *TrAC Trends in Analytical Chemistry* **2012**, *35*, 5–26.

[60] Atkins, P.; de Paula, J. *Atkin's Physical Chemistry*, 9th ed.; OUP Oxford: Oxford, UK, 2010.

[61] Olofsson, G.; Loh, W. On the Use of Titration Calorimetry to Study the Association of Surfactants in Aqueous Solutions. *Journal of the Brazilian Chemical Society* **2009**, *20*, 577–593.

[62] Loh, W.; Brinatti, C.; Tam, T. C. Use of Isothermal Titration Calorimetry to Study Surfactant Aggregation in Colloidal Systems. *Biochimica et Biophysica Acta* **2016**, *1869*, 999–1016.

[63] Knoll, M.; Ruska, E. Das Elektronenmikroskop. *Zeitschrift für Physik* **1932**, *78*, 318–339.

[64] Kisielowski, C. et al. Detection of Single Atoms and Buried Defects in Three Dimensions by Aberration-Corrected Electron Microscope with 0.5-Å Information Limit. *Microscopy and Microanalysis* **2008**, *14*, 469–477.

[65] Williams, D. B.; Carter, C. B. *Transmission Electron Microscopy: A Textbook for Materials Science*; Springer Science+Buisness Media, LLC, 2009.

[66] Brenner, S.; Horne, R. W. A Negative Staining Method for High Resolution Electron Microscopy of Viruses. *Biochimica et Biophysica Acta* **1959**, *34*, 103–110.

[67] Talmon, Y. Staining and Drying-Induced Artifacts in Electron Microscopy of Surfactant Dispersions. *Journal of Colloid and Interface Science* **1983**, *93*, 366–382.

[68] Adrian, M.; Dubochet, J.; Lepault, J.; McDowall, A. W. Cryo-Electron Microscopy of Viruses. *Nature* **1984**, *308*, 32–36.

[69] Woody, R. W. In *Methods in Enzymology*; Sauer, K., Ed.; Biochemical Spectroscopy; Academic Press, 1995; Vol. 246; pp 34–71.

[70] Kelly, S. M.; Jess, T. J.; Price, N. C. How to Study Proteins by Circular Dichroism. *Biochimica et Biophysica Acta* **2005**, *1751*, 119–139.

[71] Castelletto, V.; Hamely, I. W. In *Peptide Self-Assembly: Methods and Protocols*; Nilsson, B. L., Doran, T. M., Walker, J. M., Eds.; Methods in Molecular Biology 1777; Springer Science+Buisness Media, LLC: New York, 2018; pp 3–21.

[72] Bucak, S.; Cenker, C.; Nasir, I.; Olsson, U.; Zackrisson, M. Peptide Nanotube Nematic Phase. *Langmuir* **2009**, *25*, 4262–4265.

[73] Castelletto, V.; Nutt, D. R.; Hamley, I. W.; Bucak, S.; Cenker, Ç.; Olsson, U. Structure of Single-Wall Peptide Nanotubes: In Situ Flow Aligning X-Ray Diffraction. *Chemical Communications* **2010**, *46*, 6270–6272.

[74] Middleton, D. A.; Madine, J.; Castelletto, V.; Hamley, I. W. Insights into the Molecular Architecture of a Peptide Nanotube Using FTIR and Solid-State NMR Spectroscopic Measurements on an Aligned Sample. *Angewandte Chemie International Edition* **2013**, *52*, 10537–10540.

[75] Rüter, A.; Kuczera, S.; Pochan, D. J.; Olsson, U. Twisted Ribbon Aggregates in a Model Peptide System. *Langmuir* **2019**, *35*, 5802–5808.

[76] Kuczera, S.; Rüter, A.; Roger, K.; Olsson, U. Two Dimensional Oblique Molecular Packing within a Model Peptide Ribbon Aggregate. *accepted ChemPhysChem* **2020**,

[77] Gubitosi, M.; Travaglini, L.; di Gregorio, M. C.; Pavel, N. V.; Vázquez Tato, J.; Sennato, S.; Olsson, U.; Schillén, K.; Galantini, L. Tailoring Supramolecular Nanotubes by Bile Salt Based Surfactant Mixtures. *Angewandte Chemie International Edition* **2015**, *54*, 7018–7021.

[78] Valéry, C.; Paternostre, M.; Robert, B.; Gulik-Krzywicki, T.; Narayanan, T.; Dedieu, J.-C.; Keller, G.; Torres, M.-L.; Cherif-Cheikh, R.; Calvo, P.; Artzner, F. Biomimetic Organization: Octapeptide Self-Assembly into Nanotubes of Viral Capsid-like Dimension. *Proceedings of the National Academy of Sciences of the United States of America* **2003**, *100*, 10258–10262.

[79] Mizuta, R. et al. Dynamic Self-Assembly of DNA Minor Groove-Binding Ligand DB921 into Nanotubes Triggered by an Alkali Halide. *Nanoscale* **2018**, *10*, 5550–5558.

[80] Landman, J.; Ouhajji, S.; Prévost, S.; Narayanan, T.; Groenewold, J.; Philipse, A. P.; Kegel, W. K.; Petukhov, A. V. Inward Growth by Nucleation: Multiscale Self-Assembly of Ordered Membranes. *Science Advances* **2018**, *4*, eaat1817.

[81] Petkova, A. T.; Leapman, R. D.; Guo, Z.; Yau, W.-M.; Mattson, M. P.; Tycko, R. Self-Propagating, Molecular-Level Polymorphism in Alzheimer's ß-Amyloid Fibrils. *Science* **2005**, *307*, 262–265.

[82] Adamcik, J.; Mezzenga, R. Adjustable Twisting Periodic Pitch of Amyloid Fibrils. *Soft Matter* **2011**, *7*, 5437–5443.

[83] Adamcik, J.; Mezzenga, R. Amyloid Polymorphism in the Protein Folding and Aggregation Energy Landscape. *Angewandte Chemie International Edition* **2018**, *57*, 8370–8382.

[84] Hwang, S.; Shao, Q.; Williams, H.; Hilty, C.; Gao, Y. Q. Methanol Strengthens Hydrogen Bonds and Weakens Hydrophobic Interactions in Proteins – A Combined Molecular Dynamics and NMR Study. *The Journal of Physical Chemistry B* **2011**, *115*, 6653–6660.

[85] Klotz, I. M.; Franzen, J. S. Hydrogen Bonds between Model Peptide Groups in Solution. *Journal of the American Chemical Society* **1962**, *84*, 3461–3466.

[86] Markov, I. V. *Crystal Growth for Beginners: Fundamentals of Nucleation, Crystal Growth and Epitaxy*, 2nd ed.; World Scientific Publishing Co. Pte. Ltd.: Singapore, 2008.

[87] Arias, R. J.; Kaiser, J. T.; Rees, D. C. The "Speed Limit" for Macromolecular Crystal Growth. *Protein Science : A Publication of the Protein Society* **2018**, *27*, 1837–1841.

[88] Lindfors, L.; Forssén, S.; Westergren, J.; Olsson, U. Nucleation and Crystal Growth in Supersaturated Solutions of a Model Drug. *Journal of Colloid and Interface Science* **2008**, *325*, 404–413.

[89] Vekilov, P. G. Elementary Processes of Protein Crystal Growth. *Progress in Crystal Growth and Characterization of Materials* **1993**, *26*, 25–49.

[90] Malkin, A. J.; Kuznetsov, Y. G.; McPherson, A. In Situ Atomic Force Microscopy Studies of Surface Morphology, Growth Kinetics, Defect Structure and Dissolution in Macromolecular Crystallization. *Journal of Crystal Growth* **1999**, *196*, 471–488.

[91] Cohen, S. I. A.; Linse, S.; Luheshi, L. M.; Hellstrand, E.; White, D. A.; Rajah, L.; Otzen, D. E.; Vendruscolo, M.; Dobson, C. M.; Knowles, T. P. J. Proliferation of Amyloid-*Bl*42 Aggregates Occurs through a Secondary Nucleation Mechanism. *Proceedings of the National Academy of Sciences* **2013**, *110*, 9758–9763.

[92] Liu, G.; Gaines, J. C.; Robbins, K. J.; Lazo, N. D. Kinetic Profile of Amyloid Formation in the Presence of an Aromatic Inhibitor by Nuclear Magnetic Resonance. *ACS Medicinal Chemistry Letters* **2012**, *3*, 856–859.

[93] Irbäck, A.; Mitternacht, S.; Mohanty, S. An Effective All-Atom Potential for Proteins. *PMC Biophysics* **2009**, *2*.

[94] Kabiri, M.; Bushnak, I.; McDermot, M. T.; Unsworth, L. D. Toward a Mechanistic Understanding of Ionic Self-Complementary Peptide Self-Assembly: Role of Water Molecules and Ions. *Biomacromolecules* **2013**, *14*, 3943–3950.

[95] Lakshminarayanan, R.; Vivekanandan, S.; Samy, R. P.; Banerjee, Y.; Chi-Jin, E. O.; Teo, K. W.; Jois, S. D. S.; Kini, R. M.; Valiyaveettil, S. Structure, Self-Assembly, and Dual Role of a β-Defensin-like Peptide from the Chinese Soft-Shelled Turtle Eggshell Matrix. *Journal of the American Chemical Society* **2008**, *130*, 4660–4668.

[96] Swanekamp, R. J.; DiMaio, J. T. M.; Bowerman, C. J.; Nilsson, B. L. Coassembly of Enantiomeric Amphipathic Peptides into Amyloid-Inspired Rippled β-Sheet Fibrils. *Journal of the American Chemical Society* **2012**, *134*, 5556–5559.

[97] Noyes, A. A.; Whitney, W. R. The Rate of Solution of Solid Substances in Their Own Solutions. *Journal of the American Chemical Society* **1897**, *19*, 930–934.

[98] Kabalnov, A. S.; Shchukin, E. D. Ostwald Ripening Theory: Applications to Fluorocarbon Emulsion Stability. *Advances in Colloid and Interface Science* **1992**, *38*, 69–97.

[99] Israelachvili, J. N. *Intermolecular and Surface Forces*, 3rd ed.; Academic Press: Burlington, MA, 2011.

[100] Jeppesen, M. D.; Westh, P.; Otzen, D. E. The Role of Protonation in Protein Fibrillation. *FEBS Letters* **2010**, *584*, 780–784.

[101] Milne, J. B.; Parker, T. J. Dissociation Constant of Aqueous Trifluoroacetic Acid by Cryoscopy and Conductivity. *Journal of Solution Chemistry* **1981**, *10*, 479–487.

[102] Solomon, M. J.; Spicer, P. T. Microstructural Regimes of Colloidal Rod Suspensions, Gels, and Glasses. *Soft Matter* **2010**, *6*, 1391–1400.

[103] Yokoi, H.; Kinoshita, T.; Zhang, S. Dynamic Reassembly of Peptide RADA16 Nanofiber Scaffold. *Proceedings of the National Academy of Sciences* **2005**, *102*, 8414–8419.

[104] Kang, K.; Dhont, J. K. G. Glass Transition in Suspensions of Charged Rods: Structural Arrest and Texture Dynamics. *Physical Review Letters* **2013**, *110*, 015901.

[105] MacKintosh, F. C.; Käs, J.; Janmey, P. A. Elasticity of Semiflexible Biopolymer Networks. *Physical Review Letters* **1995**, *75*, 4425–4428.

[106] Seilheimer, B.; Bohrmann, B.; Bondolfi, L.; Muller, F.; Stuber, D.; Dobeli, H. The Toxicity of the Alzheimer's Beta-Amyloid Peptide Correlates with a Distinct Fiber Morphology. *Journal of Structural Biology* **1997**, *119*, 59–71.

[107] Doi, M.; Edwards, S. F. Dynamics of Rod-like Macromolecules in Concentrated Solution. Part 1. *Journal of the Chemical Society, Faraday Transactions 2: Molecular and Chemical Physics* **1978**, *74*, 560–570.

[108] Berne, B. J.; Pecora, R. *Dynamic Light Scattering : With Applications to Chemistry, Biology, and Physics*; Wiley, 1976.

[109] Poon, W. C. K. Colloidal Glasses. *MRS Bulletin* **2004**, *29*, 96–99.

[110] Pusey, P. N.; van Megen, W. Phase Behaviour of Concentrated Suspensions of Nearly Hard Colloidal Spheres. *Nature* **1986**, *320*, 340–342.

[111] Van Rie, J.; Schütz, C.; Gençer, A.; Lombardo, S.; Gasser, U.; Kumar, S.; Salazar-Alvarez, G.; Kang, K.; Thielemans, W. Anisotropic Diffusion and Phase Behavior of Cellulose Nanocrystal Suspensions. *Langmuir* **2019**, *35*, 2289–2302.

[112] Pusey, P. N.; Fijnaut, H. M.; Vrij, A. Mode Amplitudes in Dynamic Light Scattering by Concentrated Liquid Suspensions of Polydisperse Hard Spheres. *The Journal of Chemical Physics* **1982**, *77*, 4270–4281.

[113] Hattori, Y.; Ushiki, H.; Courbin, L.; Panizza, P. Slow Relaxation Mode in Concentrated Oil-in-Water Microemulsions Consisting of Repulsive Droplets. *Physical Review E* **2007**, *75*, 021504.

[114] Doi, M. *Soft Matter Physics*; OUP Oxford, 2013.

[115] Owczarz, M.; Casalini, T.; Motta, A. C.; Morbidelli, M.; Arosio, P. Contribution of Electrostatics in the Fibril Stability of a Model Ionic-Complementary Peptide. *Biomacromolecules* **2015**, *16*, 3792–3801.

[116] Yan, H.; Frielinghaus, H.; Nykanen, A.; Ruokolainen, J.; Saiani, A.; Miller, A. F. Thermoreversible Lysozyme Hydrogels: Properties and an Insight into the Gelation Pathway. *Soft Matter* **2008**, *4*, 1313–1325.

[117] Cao, Y.; Bolisetty, S.; Adamcik, J.; Mezzenga, R. Elasticity in Physically Cross-Linked Amyloid Fibril Networks. *Physical Review Letters* **2018**, *120*, 158103.

[118] Jones, J. L.; Marques, C. M. Rigid Polymer Network Models. *Journal de Physique* **1990**, *51*, 1113–1127.

[119] Boothroyd, S.; F. Miller, A.; Saiani, A. From Fibres to Networks Using Self-Assembling Peptides. *Faraday Discussions* **2013**, *166*, 195–207.

[120] Pääkkö, M.; Ankerfors, M.; Kosonen, H.; Nykänen, A.; Ahola, S.; Österberg, M.; Ruokolainen, J.; Laine, J.; Larsson, P. T.; Ikkala, O.; Lindström, T. Enzymatic Hydrolysis Combined with Mechanical Shearing and High-Pressure Homogenization for Nanoscale Cellulose Fibrils and Strong Gels. *Biomacromolecules* **2007**, *8*, 1934–1941.

[121] Hill, R. J. Elastic Modulus of Microfibrillar Cellulose Gels. *Biomacromolecules* **2008**, *9*, 2963–2966.

[122] Knowles, T. P.; Fitzpatrick, A. W.; Meehan, S.; Mott, H. R.; Vendruscolo, M.; Dobson, C. M.; Welland, M. E. Role of Intermolecular Forces in Defining Material Properties of Protein Nanofibrils. *Science* **2007**, *318*, 1900–1903.

[123] Sasaki, N.; Saitoh, Y.; Sharma, R. K.; Furusawa, K. Determination of the Elastic Modulus of β-Lactoglobulin Amyloid Fibrils by Measuring the Debye-Waller Factor. *International Journal of Biological Macromolecules* **2016**, *92*, 240–245.

[124] Semerdzhiev, S. A.; Lindhoud, S.; Stefanovic, A.; Subramaniam, V.; van der Schoot, P.; Claessens, M. M. A. E. Hydrophobic-Interaction-Induced Stiffening of {α}-Synuclein Fibril Networks. *Physical Review Letters* **2018**, *120*, 208102.

[125] Li, W.; Persson, B. A.; Morin, M.; Behrens, M. A.; Lund, M.; Zackrisson Oskolkova, M. Charge-Induced Patchy Attractions between Proteins. *The Journal of Physical Chemistry B* **2015**, *119*, 503–508.

[126] Stradner, A.; Sedgwick, H.; Cardinaux, F.; Poon, W. C. K.; Egelhaaf, S. U.; Schurtenberger, P. Equilibrium Cluster Formation in Concentrated Protein Solutions and Colloids. *Nature* **2004**, *432*, 492–495.

[127] Philipse, A. P.; Wierenga, A. M. On the Density and Structure Formation in Gels and Clusters of Colloidal Rods and Fibers. *Langmuir* **1998**, *14*, 49–54.

[128] Hirst, L. S. *Fundamentals of Soft Matter Science*; CRC Press, Taylor & Francis Group: Boca Raton, FL, 2013.

[129] Onsager, L. The Effects of Shape on the Interaction of Colloidal Particles. *Annals of the New York Academy of Sciences* **1949**, *51*, 627–659.

[130] Hamley, I. W. Liquid Crystal Phase Formation by Biopolymers. *Soft Matter* **2010**, *6*, 1863–1871.

[131] Stroobants, A.; Lekkerkerker, H. N. W.; Odijk, T. Effect of Electrostatic Interaction on the Liquid Crystal Phase Transition in Solutions of Rodlike Polyelectrolytes. *Macromolecules* **1986**, *19*, 2232–2238.

[132] Lang, C.; Kohlbrecher, J.; Porcar, L.; Radulescu, A.; Sellinghoff, K.; Dhont, J. K. G.; Lettinga, M. P. Microstructural Understanding of the Length- and Stiffness-Dependent Shear Thinning in Semidilute Colloidal Rods. *Macromolecules* **2019**, *52*, 9604–9612.

[133] Yan, C.; Altunbas, A.; Yucel, T.; Nagarkar, R. P.; Schneider, J. P.; Pochan, D. J. Injectable Solid Hydrogel: Mechanism of Shear-Thinning and Immediate Recovery of Injectable β-Hairpin Peptide Hydrogels. *Soft Matter* **2010**, *6*, 5143–5156.

[134] Pallbo, J.; Sparr, E.; Olsson, U. Aggregation Behavior of the Amyloid Model Peptide NACore. *Quarterly Reviews of Biophysics* **2019**, *52*, 1–10.

[135] Colvin, M. T.; Silvers, R.; Ni, Q. Z.; Can, T. V.; Sergeyev, I.; Rosay, M.; Donovan, K. J.; Michael, B.; Wall, J.; Linse, S.; Griffin, R. G. Atomic Resolution Structure of Monomorphic Aβ42 Amyloid Fibrils. *Journal of the American Chemical Society* **2016**, *138*, 9663–9674.

Printed by Media-Tryck, Lund 2020 NORDIC SWAN ECOLABEL 3041 0903

LUND UNIVERSITY

ISBN: 978-91-7422-722-2

Physical Chemistry
Faculty of Science
Lund University